



A Resource utilization method for volatile organic compounds emission from the semiconductor industry: Selective catalytic oxidation of isopropanol to acetone Over Au/ α -Fe₂O₃ nanosheets

Honghong Zhang^a, Lingyun Dai^b, Yuan Feng^a, Yuhan Xu^a, Yuxi Liu^a, Guangsheng Guo^a, Hongxing Dai^a, Chongchen Wang^c, Can Wang^d, Hsing-Cheng Hsi^e, Haibao Huang^f, Jiguan Deng^{a,*}

^a Key Laboratory of Beijing on Regional Air Pollution Control, Beijing Key Laboratory for Green Catalysis and Separation, and College of Environmental and Energy Engineering, Beijing University of Technology, Beijing 100124, China

^b Department of Mechanical Engineering, Carnegie Mellon University, Pittsburgh, Pennsylvania 15213, United States

^c Beijing Key Laboratory of Functional Materials for Building Structure and Environment Remediation, Beijing University of Civil Engineering and Architecture, Beijing 100044, China

^d School of Environmental Science and Engineering, Tianjin University, Tianjin 300350, China

^e Graduate Institute of Environmental Engineering, National Taiwan University, Taipei 10617, Taiwan

^f School of Environmental Science and Engineering, Sun Yat-Sen University, Guangzhou 510275, China

ARTICLE INFO

Keywords:

Volatile organic compounds
Resource utilization
Selective catalytic oxidation
 α -Fe₂O₃ nanosheet
Supported Au nanocatalysts

ABSTRACT

We prepare α -Fe₂O₃ nanosheet supported 0.38, 0.81, and 1.36 wt% Au (average particle size = 4.0 nm) nanocatalysts, and investigate their performance and mechanism for the selective catalytic oxidation of isopropanol to acetone. In the presence of 1.2 vol% isopropanol and 40 vol% O₂, 1.36 wt% Au/ α -Fe₂O₃ exhibits excellent catalytic performance, due to its moderate acidic sites and better redox properties, with acetone selectivity and yield being as high as 99% and 95% at 220 °C, respectively. In addition to acetone, little propylene, acetic acid, acetaldehyde, methyl vinyl ketone, 2-butanone, isopropyl ether, isopropyl acetate, 3-penten-2-one, isopropyl acrylate, isopropyl propionate, and 2, 4-dimethylfuran are detected. The possible reaction mechanism is proposed for the selective catalytic oxidation of isopropanol to acetone over the present catalysts. We believe the present selective catalytic oxidation method, rather than the traditional complete catalytic oxidation method, provides an alternative and economic method for VOCs emissions control.

1. Introduction

The semiconductor industry plays an important role in promoting social and economic development. However, some environmental problems caused by the large scale production of electronic products could not be overlooked. Semiconductor devices are manufactured via the complex production processes, involving the high frequency generation and emission of hazardous pollutants. Among the volatile organic compounds (VOCs) emitted from the semiconductor industry, in addition to little benzene, toluene, xylene, ethyl acetate, and styrene, isopropanol and acetone are the major components [1,2], because isopropanol and acetone are widely used as cleaning agents. Under sunlight irradiation, ozone and secondary organic aerosols might be produced by the photochemical reaction between VOCs and nitrogen oxides, resulting in elevated levels of atmospheric oxidizing capacity

and fine particulate matter concentration. Human body to prolonged exposure will raise the carcinogenic risk. Therefore, the purification of VOCs has attracted more and more attention [3–5].

Catalytic oxidation is a traditional method for VOCs purification, and VOCs could be completely oxidized into CO₂ and H₂O without secondary pollution [6,7]. Metal oxide supported noble metal (e.g. Au, Pt and Pd [8–11]) catalysts have been extensively studied due to their excellent low temperature activities. However, control VOCs emission via the catalytic oxidation needs great investment. In order to improve the enthusiasm of the enterprise owners for environmental protection, it is highly desired to develop a novel efficient method for the treatment of air pollution with extra economic benefits.

Haruta et al. [12] found that Au nanoparticles loaded on transition metal oxides, such as TiO₂, α -Fe₂O₃, Co₃O₄, and NiO, exhibited excellent catalytic oxidation activities. Actually, a number of studies show

* Corresponding Author, phone: +86-10-67396118, fax: +86-10-67391983.

E-mail address: jgdeng@bjut.edu.cn (J. Deng).

<https://doi.org/10.1016/j.apcatb.2020.119011>

Received 2 December 2019; Received in revised form 4 April 2020; Accepted 14 April 2020

Available online 01 May 2020

0926-3373/ © 2020 Elsevier B.V. All rights reserved.

that the supported Au catalysts exhibit remarkable performance in various important reactions including CO oxidation and water-gas shift reactions [13,14]. α -Fe₂O₃ with various morphologies such as nanodisk [15], hollow [16], and columnar superstructure [17], modified by Au nanoparticles, have been widely used as heterogeneous catalysts and *in-situ* gas sensors. For the Au/Fe₂O₃ catalysts, their catalytic performance are associated with the morphologies [16] and crystal phases [18] of Fe₂O₃ as well as the nature of the reactants [19]. In the literature, it is rare to across the complete or selective catalytic oxidation of isopropanol over Au/ α -Fe₂O₃.

As we know, acetone has been widely used in various fields. Up to now, there are three main methods to prepare acetone. The cost of the generation of acetone via the grain fermentation is too high. The main method for acetone preparation is the oxidation of cumene synthesized from benzene and propylene, and co-production of acetone and phenol. Selective catalytic oxidation of isopropanol to acetone is an important supplementary method. In recent years, selective catalytic oxidation of isopropanol has been extensively studied. The dehydration and dehydrogenation of isopropanol produce propylene and acetone, respectively. For example, the g-C₃N₄/Ag/Ag₃PO₄ composite [20] had excellent photocatalytic activity for the selective oxidation of gaseous isopropanol, and 63 % isopropanol was mainly oxidized to acetone after 4 h irradiation. Friedel et al. [21] reported that for the selective catalytic oxidation of isopropanol over novel ex-LDH CoFe₂O₄, the corresponding yield of acetone and propylene was 40 % and 52 % at 90 % conversion of isopropanol. Due to the high demand of economic method for VOCs control and resource utilization, we herein prepare α -Fe₂O₃ nanosheet supported Au nanocatalysts, and investigate their performance and mechanism for the selective catalytic oxidation of isopropanol to acetone.

2. Experimental

2.1. Catalyst preparation

α -Fe₂O₃ nanosheets (NSs) are synthesized via a solvothermal method [22]. The preparation procedures are as follows: 1.638 g of FeCl₃·6H₂O powder is dissolved in a mixed solution of 60 mL CH₃CH₂OH and 4.2 mL H₂O. After magnetic stirring for 0.5 h, 4.8 g of CH₃COONa is added to the mixture. The above precursor solution is stirred for 1 h, and then transferred to autoclave and kept in an oven at 180 °C for 12 h. α -Fe₂O₃ NSs are obtained after centrifugal separation for five times at 8000 rpm with a mixture of ethanol and deionized water. Commercial α -Fe₂O₃ (analytical purity, > 99.0 %) is used as a reference catalyst.

x wt% Au/ α -Fe₂O₃ NSs (x = 0.38, 0.81, and 1.36) is prepared by colloidal deposition method that is assisted by polyvinyl alcohol (PVA) and NaBH₄ [23]. The mass ratio of Au to PVA is 1.5: 1, and the molar ratio of Au to NaBH₄ is 1: 5. In an ice-water bath, 1.5 mmol/L HAuCl₄ aqueous solution is added with appropriate PVA solution under stirring and dark conditions. The NaBH₄ aqueous solution is quickly injected to obtain the Au nanoparticles (NPs) colloidal solution. After stirring for 0.5 h, the appropriate amount of α -Fe₂O₃ NSs is added to the above solution. Gold colloids could be well deposited on the surface of the support after continuous magnetic stirring for 12 h. The final catalysts are obtained after centrifugal separation, washing, drying, and calcination in a muffle furnace at 300 °C for 2 h.

All the chemical reagents (analytical purity) are purchased from Sinopharm chemical reagent co. LTD and used without further purification.

2.2. Catalyst characterization

All the samples are characterized by various techniques, including X-ray diffraction (XRD), ⁵⁷Fe-Mössbauer spectra, scanning electron microscopy (SEM), transmission electron microscopy (TEM),

inductively coupled plasma atomic emission spectroscopy (ICP-AES), Brunauer-Emmett-Teller (BET) technique, CO pulse chemisorption, ammonia temperature programmed desorption (NH₃-TPD), X-ray photoelectron spectroscopy (XPS), hydrogen temperature programmed reduction (H₂-TPR), thermal analyzer-gas chromatography/mass spectrometry (GC/MS), isopropanol-*in situ* diffuse reflectance Fourier transform infrared spectroscopy (isopropanol-*in situ* DRIFTS), pyridine-*in situ* DRIFTS, isopropanol temperature programmed desorption (isopropanol-TPD), and isopropanol temperature programmed surface reaction (isopropanol-TPSR). The detailed characterization conditions are included in the Supporting Information.

2.3. Catalytic performance evaluation

The catalytic performance evaluation for the catalysts is carried out in a tubular quartz fixed-bed reactor (i. d. = 6 mm) under 0, 25, 50, 75, or 100 % of relative humidity (RH). The reactants and products are detected by gas chromatography (GC-2010, Shimadzu) with FID detector and Stabilwax®-DB column capillary column. The catalyst (about 0.050 g, 40–60 mesh) is mixed with quartz sands at a mass ratio of 1: 5 to avoid local temperature runaway, and pretreated in 20 mL/min of O₂ flow at 300 °C for 1 h. By controlling the temperature, the saturated vapor pressure of isopropanol is calculated according to the Antoine Equation, and different concentrations (0.1 vol%, 0.75 vol%, and 1.2 vol%) of isopropanol is carried out by nitrogen gas. The oxygen gas concentration is 40 vol% or 10 vol%, and the nitrogen gas is the equilibrium gas. According to the amount of catalyst, and the total flow rate of the mixture gas, the space velocity (SV) is calculated to be 20,000 mL/(g h). All the catalytic performance is performed under steady-state reaction conditions, and the data are collected for three times, with the relative standard deviation less than 0.4 %, after keeping at a given temperature for 30 min.

We also determine the relative molar correction factors according to the following procedures. Trace amounts of acetone (99.9 %) is firstly dissolved in isopropanol (99.9 %). After sampling, the corresponding peak area is detected by gas chromatography. The absolute mass correction factors are calculated according to the ratio of their mass to the peak area. On this basis, the relative mass correction factors of acetone to isopropanol could be calculated. Parallel measurements are carried out three times, and the average value is adopted. In the present study, the relative molar correction factor is 1.13. The selectivity and yield of acetone are calculated by using the relative molar correction factor (f_a) of acetone to isopropanol. The calculation formulas are as follows (a–c), where A_1 and A_2 are the peak area of isopropanol at the inlet and outlet, and A_3 is the peak area of acetone at the outlet of the reactor tube detected by GC.

- (a) Isopropanol conversion = $(A_1 - A_2)/A_1 \times 100 \%$
- (b) Acetone selectivity = $A_3 \times f_a/(A_1 - A_2) \times 100 \%$
- (c) Acetone yield = $A_3 \times f_a/A_1 \times 100 \%$

3. Results and discussion

3.1. Crystal structure, surface area, morphology, and size distribution of commercial α -Fe₂O₃, α -Fe₂O₃ NSs, and x wt% Au/ α -Fe₂O₃ NSs

The actual Au contents of present x wt% Au/ α -Fe₂O₃ NSs are 0.38, 0.81, and 1.36 wt%, determined by ICP-AES (Table S1). According to the standard card (JCPDS PDF# 33–0664), we find that the XRD patterns of commercial α -Fe₂O₃, and the as-prepared α -Fe₂O₃ NSs and x wt% Au/ α -Fe₂O₃ NSs exhibit typical characteristic of rhombohedral α -Fe₂O₃ (Fig. S1). Compared with commercial α -Fe₂O₃, α -Fe₂O₃ NSs and x wt% Au/ α -Fe₂O₃ NSs exhibit wider diffraction peaks and lower relative strength, due to the increase of lattice strain and the decrease of grain size [24]. Lattice strain might cause the increase of surface defects, which benefits the reactant adsorption. The grain sizes of the α -Fe₂O₃ NSs supports are 35.7–43.2 nm (Table S1) for the as-obtained

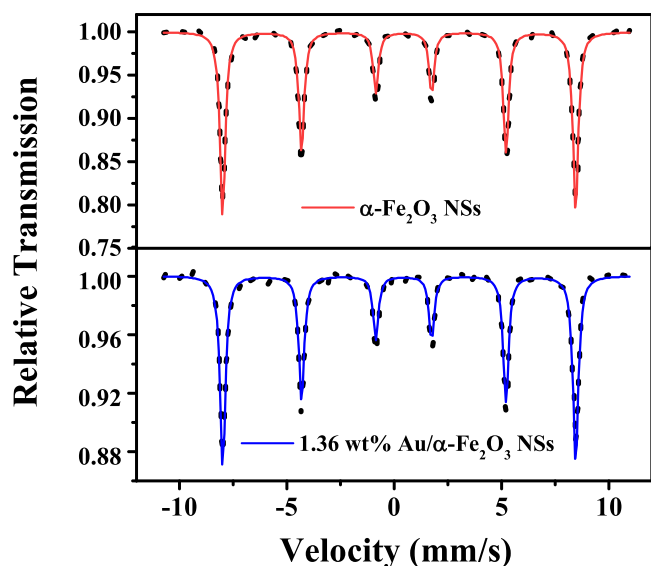


Fig. 1. Mössbauer spectra recorded at room temperature, and the fitting (solid curve) of the spectra.

catalysts, much smaller than that for commercial α -Fe₂O₃. Accordingly, the surface areas of α -Fe₂O₃ NSs and x wt% Au/ α -Fe₂O₃ NSs (12.6–18.4 m²/g) are much larger than that of commercial α -Fe₂O₃ (4.3 m²/g). The ⁵⁷Fe-Mössbauer spectra (Fig. 1) show that the peak shapes of the α -Fe₂O₃ NSs and 1.36 wt% Au/ α -Fe₂O₃ NSs samples are identical. The fitting curves show one sextet of magnetic splitting, which is consistent with the spectra of standard α -Fe₂O₃ without impurities. Compared with the support, the relative absorption intensity of 1.36 wt% Au/ α -Fe₂O₃ NSs decreases and the line width increases, indicating that the crystallinity of α -Fe₂O₃ NSs drops, which is consistent with the results of XRD. Combining with the parameters of hyperfine interaction in Table S2, it is also clear that the isomer shift, quadrupole splitting and hyperfine magnetic field of the two samples are identical, implying that the chemical environment of atoms in the support is not altered by Au NPs loading, but the line width rises slightly. The modification of Au NPs decreases the long-range order and increases the disorder of α -Fe₂O₃ NSs. From the perspective of catalysis, it means that there are more defect sites on the support. In general, the defect of support is the active center, hence the catalytic performance might be enhanced. Au NPs are highly dispersed on the surface of the support, and there is no diffraction peak due to Au species. SEM image (Fig. S2a) shows that the α -Fe₂O₃ nanocrystals display regular hexagonal morphology, and the width and thickness are about 180 and 15 nm, respectively. TEM images (Fig. S2b–f) confirm that Au NPs are well dispersed on the surface of α -Fe₂O₃ NSs. The interplanar spacing of the α -Fe₂O₃ NSs is ca. 0.251 nm, corresponding to the (110) crystal plane in the standard card (JCPDS PDF# 33–0664). The interplanar spacing of the Au NPs is ca. 0.232 nm, due to the (111) crystal plane in the standard card (JCPDS PDF# 04–0784). The average Au particle size of the 0.38,

0.81, and 1.36 wt% Au/ α -Fe₂O₃ NSs is 4.2, 4.3, and 3.8 nm (Fig. S3 and Table S1), respectively.

3.2. Surface composition, reducibility, and surface acidity of commercial α -Fe₂O₃, α -Fe₂O₃ NSs, and x wt% Au/ α -Fe₂O₃ NSs

Shown in Fig. S4 are the Fe 2p, O 1s, and Au 4f XPS spectra of α -Fe₂O₃ NSs and Au/ α -Fe₂O₃ NSs. In the Fe 2p XPS spectra (Fig. S4A), there are two asymmetric peaks, due to the 2p_{3/2} and 2p_{1/2} orbits, respectively. Each orbit could be divided into four parts at different binding energies (BEs). For the Fe 2p_{3/2} orbit, the signals at BEs = 709.6 and 714.3 eV, and BEs = 711.2 and 718.5 eV, could be due to Fe²⁺ and Fe³⁺, respectively. For the Fe 2p_{1/2} orbit, the signals at BEs = 722.7 and 727.1 eV, and BEs = 724.4 and 732.3 eV, could be due to Fe²⁺ and Fe³⁺ [25,26], respectively. The presence of Fe²⁺ on the surface might be partially associated with the weak reduction of Fe³⁺ by ethanol used in the preparation process. The O 1s XPS spectra (Fig. S4B) could be divided into three parts at BEs = 529.4, 531.1, and 532.9 eV, due to the surface lattice oxygen (O_{latt}), surface adsorbed oxygen (O_{ads}), and surface hydroxyl species [27], respectively. The Au 4f XPS spectra (Fig. S4C) could be divided into four parts at BEs = 83.9 and 87.6 eV, and BEs = 84.9 and 88.6 eV. The former two could be due to Au⁰ species, and the latter two could be due to Au^{δ+} (e.g., Au⁺ or Au³⁺) species [15]. As shown in Table 1, the surface Fe³⁺/Fe²⁺ molar ratio decreases from 2.67 to 1.96, while the surface Au^{δ+}/Au⁰ molar ratio increases from 0.23 to 0.31, due to the interaction (Au⁰ + Fe³⁺ → Au^{δ+} + Fe²⁺) between Au NPs and α -Fe₂O₃ NSs, with a rise in the Au loading from 0 to 1.36 wt%. Furthermore, the surface O_{ads}/O_{latt} molar ratio also increases from 0.24 to 0.38.

Fig. 2 gives the H₂-TPR profiles of commercial α -Fe₂O₃, α -Fe₂O₃ NSs and Au/ α -Fe₂O₃ NSs. Clearly, there are two main reduction peaks in the range of 250 – 450 °C and 450 – 750 °C over the present catalysts. For the commercial α -Fe₂O₃ and α -Fe₂O₃ NSs, the peak I corresponds to the reduction of Fe₂O₃ to Fe₃O₄, and the peak II corresponds to the reduction of Fe₃O₄ → FeO → Fe⁰ [18]. Compared with that over commercial α -Fe₂O₃, the temperature of peak I over α -Fe₂O₃ NSs decreases from 394 to 372 °C, indicating a slight improvement in low temperature reducibility. Moreover, the loading of Au NPs onto α -Fe₂O₃ NSs could further enhance the low temperature reducibility. The temperature of peak I over 0.38, 0.81, and 1.36 wt% Au/ α -Fe₂O₃ NSs is 336, 299, and 267 °C, respectively. The decrease in the initial reduction temperature is associated with the interaction (Au⁰ + Fe³⁺ → Au^{δ+} + Fe²⁺) between Au NPs and α -Fe₂O₃ NSs. Such interaction not only gives rise to the generation of Au^{δ+}, but also lengthens the distance between Fe and O atoms, and weakens the Fe–O bond. In addition to the reduction of Fe₂O₃ to Fe₃O₄, the peak I over Au/ α -Fe₂O₃ NSs also corresponds to the reduction of Au^{δ+} to Au⁰. The total H₂ consumption of α -Fe₂O₃ NSs and Au/ α -Fe₂O₃ NSs is in the range of 18.54 – 22.12 mmol/g (Table 1). It should be noted that due to the generation of more Fe²⁺ species and surface defects, the total H₂ consumption of x wt% Au/ α -Fe₂O₃ NSs is lower than that of α -Fe₂O₃ NSs, and slightly decreases with an increase in the Au loading.

In order to determine the surface acidity of commercial α -Fe₂O₃, α -

Table 1
Surface element compositions and H₂ consumption of different catalysts.

Catalyst	Surface element composition (mol/mol) ^a			Actual H ₂ consumption (mmol/g) ^b		
	Fe ³⁺ /Fe ²⁺	O _{ads} /O _{latt}	Au ^{δ+} /Au ⁰	Peak I	Peak II	Total
α -Fe ₂ O ₃ NSs	2.67	0.24	–	2.16	19.96	22.12
0.38 wt% Au/ α -Fe ₂ O ₃ NSs	2.49	0.26	0.23	1.98	17.79	19.77
0.81 wt% Au/ α -Fe ₂ O ₃ NSs	2.07	0.34	0.26	2.03	16.67	18.70
1.36 wt% Au/ α -Fe ₂ O ₃ NSs	1.96	0.38	0.31	2.05	16.49	18.54

^a Determined from XPS.

^b Determined from H₂-TPR.

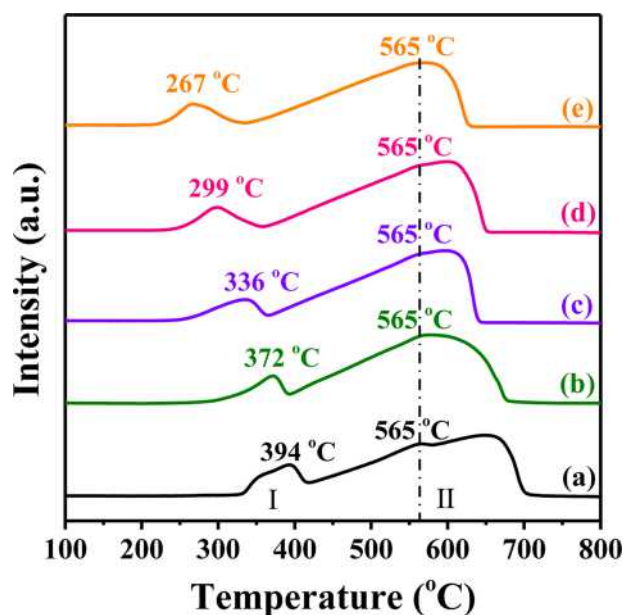


Fig. 2. H_2 -TPR profiles of (a) commercial $\alpha\text{-Fe}_2\text{O}_3$, (b) $\alpha\text{-Fe}_2\text{O}_3$ NSs, (c) 0.38 wt % Au/ $\alpha\text{-Fe}_2\text{O}_3$ NSs, (d) 0.81 wt% Au/ $\alpha\text{-Fe}_2\text{O}_3$ NSs, and (e) 1.36 wt% Au/ $\alpha\text{-Fe}_2\text{O}_3$ NSs.

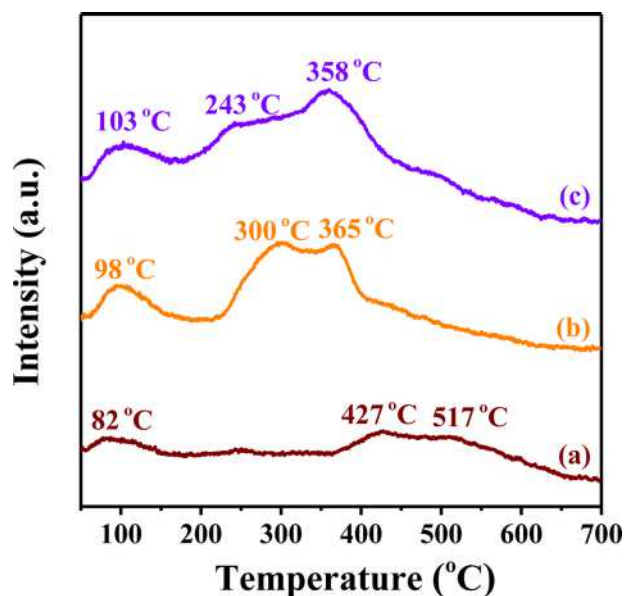


Fig. 3. NH_3 -TPD profiles over (a) commercial $\alpha\text{-Fe}_2\text{O}_3$, (b) $\alpha\text{-Fe}_2\text{O}_3$ NSs, and (c) 1.36 wt% Au/ $\alpha\text{-Fe}_2\text{O}_3$ NSs.

Fe_2O_3 NSs and 1.36 wt% Au/ $\alpha\text{-Fe}_2\text{O}_3$ NSs, we carry out the NH_3 -TPD and pyridine-*in situ* DRIFTS experiments. Fig. 3 gives the NH_3 -TPD profiles over different catalysts. The peaks located at 80 – 100 °C corresponds to the desorption of physical adsorbed NH_3 . The broad peaks over commercial $\alpha\text{-Fe}_2\text{O}_3$ at 427 and 517 °C could be due to the desorption of NH_3 adsorbed at strong acidic sites [28]. The peaks over $\alpha\text{-Fe}_2\text{O}_3$ NSs at 300 and 365 °C could be due to the desorption of NH_3 adsorbed at moderate acidic sites. The peaks over 1.36 wt% Au/ $\alpha\text{-Fe}_2\text{O}_3$ NSs at 243 and 358 °C is attributed to the desorption of NH_3 adsorbed at weak and moderate acidic sites, respectively. The desorption amount of NH_3 over commercial $\alpha\text{-Fe}_2\text{O}_3$ is 16 $\mu\text{mol/g}$, much less than that over (62 $\mu\text{mol/g}$) $\alpha\text{-Fe}_2\text{O}_3$ NSs and (74 $\mu\text{mol/g}$) 1.36 wt% Au/ $\alpha\text{-Fe}_2\text{O}_3$ NSs (Table 2). The large difference in the acid strength and amount might be related to the preparation method and condition of the commercial $\alpha\text{-Fe}_2\text{O}_3$ and $\alpha\text{-Fe}_2\text{O}_3$ NSs. It has been reported that the

Table 2

The acid amount of different catalysts determined by NH_3 -TPD, the amount of Lewis acid at 1450 cm^{-1} and Brønsted acid at 1540 cm^{-1} determined by pyridine adsorption.

Catalyst	Desorption of NH_3 ($\mu\text{mol/g}$)		Amount of adsorbed pyridine ($\mu\text{mol/g}$)			
	T (°C)	Total	T (°C)	Brønsted acidic site	Lewis acidic site	Brønsted/Lewis acidic site
commercial	427,	16	200	1.14	30.55	0.037
$\alpha\text{-Fe}_2\text{O}_3$	517		350	0.66	11.45	0.058
$\alpha\text{-Fe}_2\text{O}_3$ NSs	300,	62	200	2.21	43.01	0.051
	365		350	0.94	14.55	0.065
1.36 wt% Au/ $\alpha\text{-Fe}_2\text{O}_3$	243,	74	200	1.98	105.68	0.019
NSs	358		350	0.89	37.19	0.024

weak and strong acidity is mainly caused by the Lewis acid [29] and Brønsted acid [30] sites, respectively. For the purpose of further determination of acidity (e.g., Brønsted acid or Lewis acid) and acid strength, we carry out the pyridine-*in situ* DRIFTS experiment at 200 and 350 °C (Fig. 4). Generally, the band at 1450 cm^{-1} is the characteristic absorption peak of pyridine ring on the Lewis acidic site, the band at 1490 cm^{-1} is the absorption of pyridine on the Brønsted acidic and Lewis acidic sites simultaneously, the band at 1540 cm^{-1} is the characteristic absorption peak of pyridine ion on the Brønsted acidic site, the band at 1601 cm^{-1} is the absorption of pyridine on the Lewis acidic site, and the band at 1650 cm^{-1} is the absorption of protonated pyridine on the Brønsted acidic site [31]. The commercial $\alpha\text{-Fe}_2\text{O}_3$, $\alpha\text{-Fe}_2\text{O}_3$ NSs and 1.36 wt% Au/ $\alpha\text{-Fe}_2\text{O}_3$ NSs exhibit the larger amount of Lewis acid, because Fe^{3+} could provide Lewis acidic sites. Compared with that at 200 °C, the peak intensity due to the Lewis acidic site is lower at 350 °C, indicating the Lewis acid is weak and easy to remove. Table 2 shows the acid amount of the commercial $\alpha\text{-Fe}_2\text{O}_3$, $\alpha\text{-Fe}_2\text{O}_3$ NSs and 1.36 wt% Au/ $\alpha\text{-Fe}_2\text{O}_3$ NSs calculated on the basis of the pyridine-*in situ* DRIFTS experiment. It can be seen that the loading of Au onto the support greatly increases the Lewis acidic sites, and slightly decreases the Brønsted acidic sites, in consistency with the NH_3 -TPD results.

3.3. Performance for selective catalytic oxidation of isopropanol over commercial $\alpha\text{-Fe}_2\text{O}_3$, $\alpha\text{-Fe}_2\text{O}_3$ NSs, and x wt% Au/ $\alpha\text{-Fe}_2\text{O}_3$ NSs

As mentioned above, isopropanol and acetone are the major components, among the VOCs emissions from the semiconductor industry. We herein investigate the catalytic performance of $\alpha\text{-Fe}_2\text{O}_3$ NSs and Au/ $\alpha\text{-Fe}_2\text{O}_3$ NSs for the selective catalytic oxidation of isopropanol to acetone. Under the reactants composed of 0.1 vol% isopropanol and 40 vol% O_2 , with N_2 as equilibrium gas, the isopropanol conversion, acetone selectivity and yield over the present catalysts as a function of the reaction temperature is shown in Fig. S5. Over $\alpha\text{-Fe}_2\text{O}_3$ NSs, isopropanol only begins to react with O_2 at a temperature higher than 120 °C, and isopropanol conversion increases with a rise in temperature. Acetone selectivity first increases from 74 % to 93 % with a rise in temperature from 120 to 150 °C, and then slightly decreases from 93 % to 81 % with a further rise in temperature from 150 to 240 °C. Acetone yield increases with a rise in temperature below 240 °C, while greatly decreases above 240 °C, due to the significant decrease in acetone selectivity. The loading of Au NPs onto the $\alpha\text{-Fe}_2\text{O}_3$ NSs causes the selective catalytic oxidation of isopropanol to take place at room temperature (Fig. S5A). The trend of isopropanol conversion, acetone selectivity and yield over Au/ $\alpha\text{-Fe}_2\text{O}_3$ NSs is similar to that over $\alpha\text{-Fe}_2\text{O}_3$ NSs. In addition to the low reaction temperature, another big difference is the acetone selectivity over Au/ $\alpha\text{-Fe}_2\text{O}_3$ NSs could be kept at a high level in the range of room temperature to 170 °C. The 1.36 wt % Au/ $\alpha\text{-Fe}_2\text{O}_3$ NSs catalyst exhibits relatively better catalytic

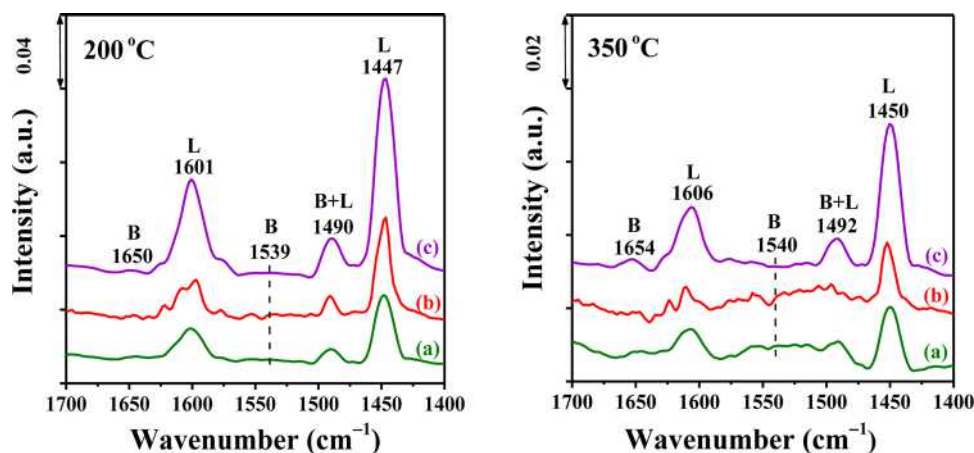


Fig. 4. Pyridine-*in situ* DRIFTS over (a) commercial α -Fe₂O₃, (b) α -Fe₂O₃ NSs, and (c) 1.36 wt% Au/ α -Fe₂O₃ NSs at 200 and 350 °C.

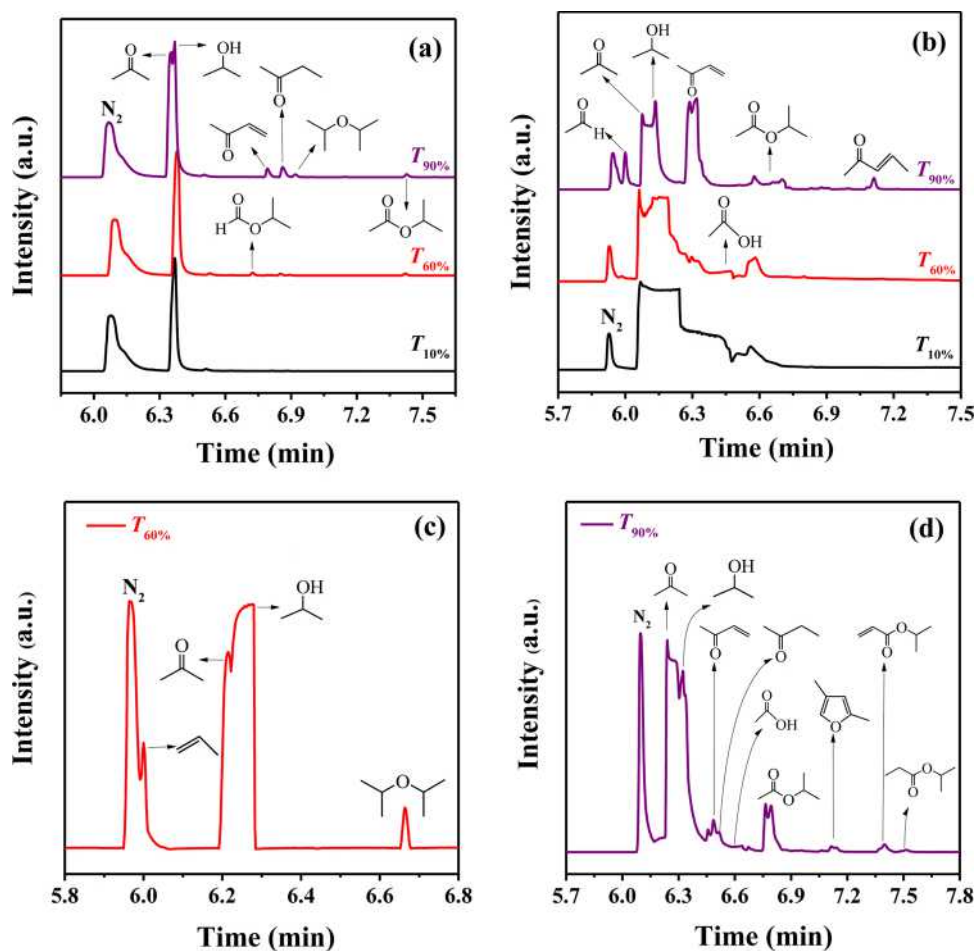


Fig. 5. Possible reaction intermediate products detected by GC-MS during the selective catalytic oxidation process with (a) 0.1 vol% and (b) 1.2 vol% isopropanol over α -Fe₂O₃ NSs, (c) 0.1 vol% isopropanol over commercial α -Fe₂O₃, and (d) 1.2 vol% isopropanol over 1.36 wt% Au/ α -Fe₂O₃ NSs.

performance for the present reaction. At room temperature, isopropanol conversion and acetone selectivity is 36.7 % and 93.3 %, respectively. In the range of 120 – 170 °C, acetone selectivity and yield are much more than 90 %. At 150 °C, the acetone yield is up to 96.2 %, where isopropanol conversion is 96.7 %, and acetone selectivity is about 99.5 % (Table S3). The Au dispersion of 0.38 wt%, 0.81 wt%, and 1.36 wt% Au/ α -Fe₂O₃ NSs, determined by the CO pulse chemisorption method, is 14.2, 19.0 and 28.6 %, respectively. Then we calculate TOF_{Au}, isopropanol consumption rate, and acetone formation rate at 30 °C.

Although TOF_{Au} ($17.8 \times 10^{-3} \text{ s}^{-1}$) of the 0.38 wt% Au/ α -Fe₂O₃ NSs catalyst is larger than these ($9.0 \times 10^{-3} \text{ s}^{-1}$ and $4.2 \times 10^{-3} \text{ s}^{-1}$) of the 0.81 wt% and 1.36 wt% Au/ α -Fe₂O₃ NSs catalysts, isopropanol consumption rate ($4.9\text{--}8.3 \times 10^{-8} \text{ mol g}_{\text{cat}}^{-1} \text{ s}^{-1}$) and acetone formation rate ($3.8\text{--}7.8 \times 10^{-8} \text{ mol g}_{\text{cat}}^{-1} \text{ s}^{-1}$) increase with a rise in the Au loading. It should be noted that acetone selectivity could not reach 100 %, due to the presence of little intermediate products, which will be discussed later. Under an oxygen-rich reaction conditions, the oxidative dehydrogenation of isopropanol, rather than the deep oxidation

of isopropanol and/or acetone, mainly occurs over 1.36 wt% Au/ α -Fe₂O₃ NSs at a low temperature.

Theoretically, 0.1 vol% isopropanol would be converted to 0.1 vol% acetone. Hence, we also investigate the catalytic activity of 1.36 wt% Au/ α -Fe₂O₃ NSs for the complete oxidation of acetone (Fig. S6), and find that the initial temperature required for acetone oxidation is 180 °C under the reactants consisted of 0.1 vol% acetone and 40 vol% O₂, with N₂ as equilibrium gas. Due to the low catalytic activity of 1.36 wt% Au/ α -Fe₂O₃ NSs for the complete oxidation of acetone, the high selectivity and yield of acetone in the range of 120 – 170 °C are understandable, for the selective catalytic oxidation of isopropanol. Nevertheless, when the reaction temperature is high enough, acetone will undergo deep oxidation (Table S4), which is the possible reason for the acetone selectivity and yield greatly decreases above 210 °C (Fig. S5).

For comparison, we also investigate the selective catalytic oxidation of isopropanol to acetone over commercial α -Fe₂O₃ (Fig. S7). Unlike that over α -Fe₂O₃ NSs, propylene is the main product, in addition to little acetone. Propylene selectivity increases with a rise in temperature below 150 °C, and then slightly decreases with a further rise in temperature from 150 to 250 °C. The highest propylene yield is 72 %, achieved at 180 °C.

3.4. Possible intermediate products generated from selective catalytic oxidation of isopropanol over commercial α -Fe₂O₃, α -Fe₂O₃ NSs, and 1.36 wt% Au/ α -Fe₂O₃ NSs

For the purpose of understanding the selective catalytic oxidation process, we try to detect the possible intermediate products by GC–MS at various temperatures over α -Fe₂O₃ NSs, commercial α -Fe₂O₃, and 1.36 wt% Au/ α -Fe₂O₃ NSs. During the evaluation of catalytic performance, the peaks detected by GC-2010 due to isopropanol and acetone are well separated, while these detected by GC–MS are not very well separated (Fig. 5). In addition, the tailed peaks also could be observed, due to the presence of several intermediate products with similar formula weight. Under the reactants composed of 0.1 vol% isopropanol ((CH₃)₂CHOH) and 40 vol% O₂, in addition to the major product acetone (CH₃COCH₃), there are isopropyl formate (HCOOCH(CH₃)₂), methyl vinyl ketone (CH₃COCH = CH₂), 2-butanone (CH₃COCH₂CH₃), isopropyl ether ((CH₃)₂CHOHC(CH₃)₂), and isopropyl acetate (CH₃COOCH(CH₃)₂) over α -Fe₂O₃ NSs at T10 %, T60 %, and/or T90 % (Fig. 5a). With a rise in the isopropanol concentration from 0.1 to 1.2 vol%, acetone is still the major product. However, some new signals due to acetic acid (CH₃COOH), acetaldehyde (CH₃CHO), and 3-penten-2-one (CH₃COCH = CHCH₃) are detected, and the intensity of the peak due to methyl vinyl ketone (CH₃COCH = CH₂) becomes much stronger at T90 %. We deduce that 3-penten-2-one is generated from the aldol condensation between CH₃COCH₃ and CH₃CHO. Propylene (CH₂=CHCH₃) is not detected over α -Fe₂O₃ NSs, possibly due to low content and weak adsorption in the enrichment tube (Fig. 5b). As mentioned above, unlike that over α -Fe₂O₃ NSs, propylene (CH₂=CHCH₃) is the main product, in addition to little acetone over commercial α -Fe₂O₃ (Fig. S7). From Fig. 5c, in addition to acetone and isopropyl ether ((CH₃)₂CHOHC(CH₃)₂), significant signal due to propylene is clearly observed at T60 % over commercial α -Fe₂O₃. In the presence of 1.2 vol% isopropanol (Fig. 5d), acetone is the major product, and propylene is not detected at T90 % over 1.36 wt% Au/ α -Fe₂O₃ NSs. Methyl vinyl ketone (CH₃COCH = CH₂), 2-butanone (CH₃COCH₂CH₃), acetic acid (CH₃COOH), and isopropyl acetate (CH₃COOCH(CH₃)₂), isopropyl acrylate (CH₂=CHCOOCH(CH₃)₂), isopropyl propionate (CH₃CH₂COOCH(CH₃)₂), and 2,4-dimethylfuran are also detected due to the various side reactions.

We also adopt the *in situ* DRIFTS technique to further investigate the selective catalytic oxidation process (Table 3 and Fig. 6). Under the reactants composed of 0.1 vol% isopropanol and 40 vol% O₂, with N₂ as equilibrium gas, isopropanol is adsorbed by commercial α -Fe₂O₃ at room temperature for 30 min, and then purged with N₂ (Fig. 6a). The

Table 3

The attribution of the *in situ* DRIFTS bands of isopropanol adsorption-desorption and selective catalytic oxidation over the present catalysts.

Frequency (cm ⁻¹)	Assignment	Group	Molecular formula	Reference
3663	ν (O–H)	isopropanol	(CH ₃) ₂ CHOH	[32]
2975–2963	ν_{as} (CH ₃)	isopropanol	(CH ₃) ₂ CHOH	[40]
2880–2878	ν_s (CH ₃)	isopropanol	(CH ₃) ₂ CHOH	[40]
1760–1728	ν (C = O)	aldehyde	R–CHO	[36,37,39]
		carboxylic acid	R–COOH	
		ester	R–COOR'	
		carbonyl		
1722–1715	ν (C = O)	acetone	CH ₃ COCH ₃	[32]
1661	ν (C = C)	propylene	CH ₂ =CHCH ₃	[34,35]
1630	ν_{as} (–COO)	carboxylate	–COO–	[22]
1472–1465	δ_{as} (CH ₃)	isopropanol	(CH ₃) ₂ CHOH	[33]
1446–1440	ν_s (COO)	acetic acid	CH ₃ COOH	[6,36]
1389–1359	δ_s (CH ₃)	isopropanol	(CH ₃) ₂ CHOH	[33]
1282	δ (O–H)	isopropanol	(CH ₃) ₂ CHOH	[32]
1231	ν_{as} (C(=O)–O–C)	acetate	CH ₃ COOR	[38]
1193	ν_{as} (C(=O)–O–C)	propionate	CH ₃ CH ₂ COOR	[38]
1164	ν (C–C)	isopropanol	(CH ₃) ₂ CHOH	[33]
1151	δ (C–O)	isopropanol	(CH ₃) ₂ CHOH	[40]
1129	ρ (CH ₃)	isopropanol	(CH ₃) ₂ CHOH	[33]
1094	ν (O–C–C)	secondary alcohol ester	CH ₃ COOCH(CH ₃) ₂	[38]
1085	ν (C–O)	isopropoxy	(CH ₃) ₂ CHO–	[37]
1015	ν (C–O)	ether	R–O–R'	[38]
957	γ (O–H)	isopropanol	(CH ₃) ₂ CHOH	[32]
907	δ (=CH ₂)	propylene	CH ₂ =CHCH ₃	[35]

absorption band at 3663 cm⁻¹ is attributed to the O–H stretching vibration (ν (OH–)) of isopropanol. The asymmetric and symmetric stretching vibrations (ν_{as} and ν_s) of CH₃ are located at 2975 and 2880 cm⁻¹. The band at 1465 cm⁻¹ and 1389 cm⁻¹ is due to the asymmetric and symmetric bending vibration (δ_{as} and δ_s) of CH₃, respectively. The weak band at 1164 cm⁻¹ is due to the skeletal C–C stretch mode (ν (CC)), and at 957 cm⁻¹ is due to the OH– out-of-plane bending vibration (γ (OH–)) of isopropanol [32,33]. Moreover, the intensities of these bands are significantly decreased after N₂ purging, indicating the adsorption of isopropanol on commercial α -Fe₂O₃ is relatively weak. With an increase in the temperature, some new bands are detected due to selective catalytic oxidation of isopropanol might happen (Fig. 6b). The band at 1359 cm⁻¹ is ascribed to the CH₃ symmetric bending vibration (δ_s) of isopropanol. The bands at 1661 and 907 cm⁻¹ are due to the CC stretching (1620–1680 cm⁻¹) vibration (ν (CC=)) and = CH₂ plane bending vibration (δ (=CH₂)) in propylene (CH₂=CHCH₃), respectively [34,35]. The band at 1440 cm⁻¹ is ascribed to symmetrical stretching vibration of acetate species (ν_s (COO)) [6,36]. The weak band at 1715 cm⁻¹ is attributed to the C=O stretching vibration (ν (CO=)) of acetone (CH₃COCH₃), and at 1085 cm⁻¹ is due to the C–O stretching vibration (ν (C–O)) of isopropoxy ((CH₃)₂CHO–), indicating the existence of isopropyl ether ((CH₃)₂CHOHC(CH₃)₂) [37].

Compared with that over commercial α -Fe₂O₃ (Fig. 6a), two new bands at 1282 cm⁻¹ due to the OH– in-plane bending vibration (δ (O–H)) of molecularly adsorbed isopropanol, and at 1129 cm⁻¹ due to the CH₃ rocking vibration (ρ (CH₃)) of adsorbed isopropanol [32,33] are detected over α -Fe₂O₃ NSs and 1.36 wt% Au/ α -Fe₂O₃ NSs (Fig. 6c and Fig. 6e), after the catalysts are pretreated by 0.1 vol% isopropanol at room temperature. In addition, there are very weak bands at 1722 cm⁻¹ and 1231 cm⁻¹ over 1.36 wt% Au/ α -Fe₂O₃ NSs, due to the C=O stretching (ν (CO=)) of ketone and the C(=O)–O–C asymmetric stretching vibration (ν_{as} (C(=O)–O–C)) of acetate [38], respectively. Such results are understandable, since 1.36 wt% Au/ α -Fe₂O₃ NSs exhibits relatively high catalytic activity for the selective catalytic oxidation at room temperature (Fig. S5). The weak band at 1630 cm⁻¹ is attributed to the carboxylate group asymmetrical stretching vibration (ν_{as} (COO)) (Fig. 6c) [22]. With an increase in the temperature, the

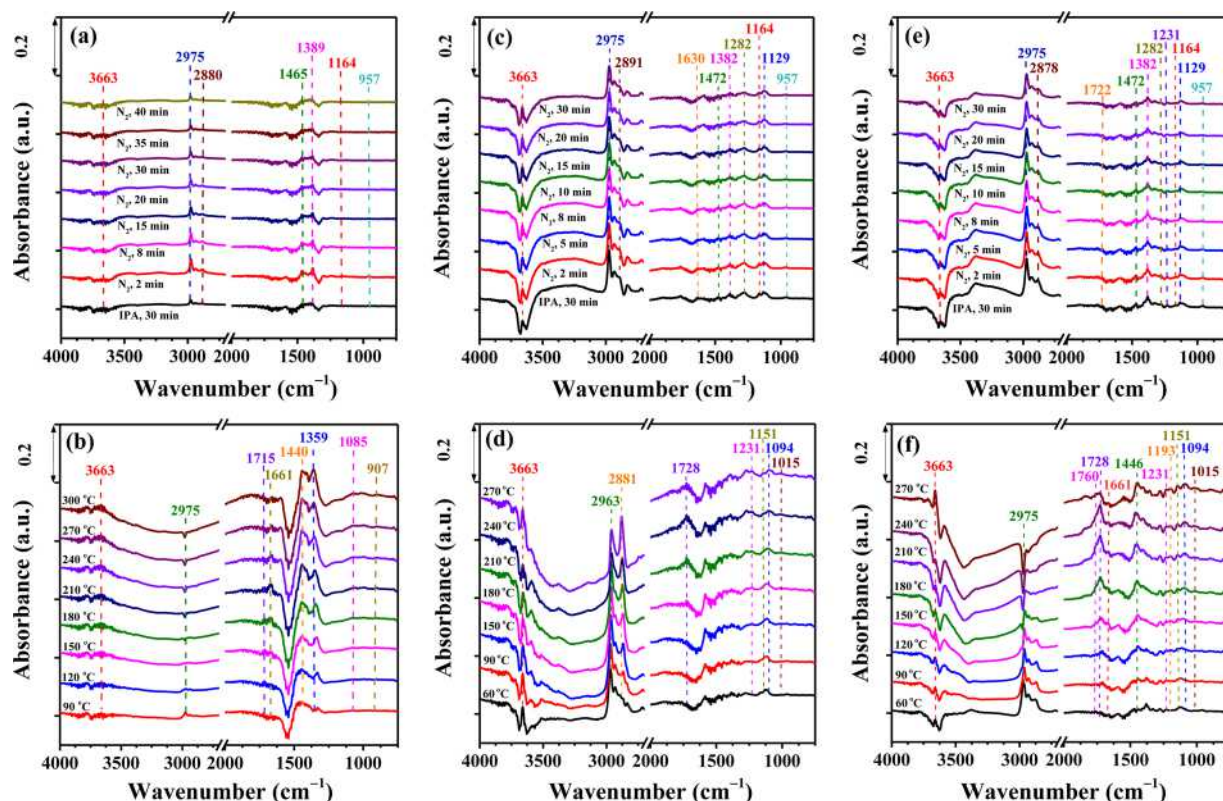


Fig. 6. *In situ* DRIFTS spectra of 0.1 vol% isopropanol adsorption-desorption at room temperature (a, c, e) and selective catalytic oxidation at different temperature (b, d, f) over (a, b) commercial α -Fe₂O₃, (c, d) α -Fe₂O₃ NSs, and (e, f) 1.36 wt% Au/ α -Fe₂O₃ NSs.

intensity of the band at 1760–1728 cm⁻¹ due to the presence of aldehyde (R-CHO), the carboxylic acid (R-COOH), and ester carbonyl groups (R-COOR') [36,37,39] become strong (Fig. 6d and Fig. 6f). It further confirms the generation of 2-butanone (CH₃COCH₂CH₃), acetaldehyde (CH₃CHO), acetic acid (CH₃COOH), isopropyl acetate (CH₃COOCH(CH₃)₂), and 3-penten-2-one (CH₃COCH=CHCH₃) (Fig. 5b). The band at 1661 cm⁻¹ (Fig. 6f) is due to the C=C stretching vibration (ν (CC)). When CO= is conjugated with C=C, π electron delocalization would occur, and weaken C=O double bond characteristic, then make the band shift to the low wavenumber. Hence, there may be methyl vinyl ketone (CH₃COCH=CH₂), isopropyl acrylate (CH₂=CHCOOCH(CH₃)₂), and 2, 4-dimethylfuran (Fig. 5d). The band at 1446 cm⁻¹ is attributed to symmetrical stretching vibration (ν_s (COO)) of acetate species, indicating the formation of acetic acid (CH₃COOH) (Fig. 6f). The bands at 1231 cm⁻¹ is attributed to the C(=O)-O-C asymmetric stretching vibration (ν_{as} (C(=O)-O-C)) of CH₃COOR, at 1151 cm⁻¹ is attributed to the C-O bending vibration (δ (C-O)) of dissociative isopropanol [40] adsorbed on the α -Fe₂O₃ NSs, and at 1094 cm⁻¹ is due to the OCC— stretching vibration (ν (OCC—)) of secondary alcohol, indicating the existence of isopropyl acetate (CH₃COOCH(CH₃)₂). As for the O-CC— stretching vibration of alcohol, here we attribute the absorption band at 1094 cm⁻¹ to the OCC— stretching vibration of secondary alcohol ester, because the O-CC— vibration band in ester is related to the type of ester. The O-CC— band of primary alcohol ester is 1064–1031 cm⁻¹, while that of secondary alcohol ester is 1100 cm⁻¹ [38]. The band at 1015 cm⁻¹ is due to the C-O stretching vibration (ν (C-O)) of ethers (R-O-R') (Fig. 6d and Fig. 6f). The band at 1193 cm⁻¹ is due to the C(=O)-O-C asymmetric stretching vibration (ν_{as} (C(=O)-O-C)) of propionate (CH₃CH₂COOR) [38]. To be exact, the present propionate is isopropyl propionate (CH₃CH₂COOCH(CH₃)₂) detected by GC-MS.

It should be noted that although high acetone selectivity and yield could be achieved over 1.36 wt% Au/ α -Fe₂O₃ NSs under certain

reaction conditions, the possible little residual products, including propylene, acetic acid, acetaldehyde, methyl vinyl ketone, 2-butanone, isopropyl ether, isopropyl acetate, 3-penten-2-one, isopropyl acrylate, isopropyl propionate, and 2, 4-dimethylfuran, would cause harmful effect on human health (Table S5). Therefore, it is important to take necessary measures (e.g. activated carbon adsorption) to remove these products.

3.5. Adsorption, activation, and transformation behaviors of isopropanol over commercial α -Fe₂O₃, α -Fe₂O₃ NSs, and x wt% Au/ α -Fe₂O₃ NSs

In order to investigate the adsorption, activation, and transformation behaviors of isopropanol, we carry out the isopropanol temperature programmed desorption (isopropanol-TPD) (Fig. 7) and isopropanol temperature programmed surface reaction (isopropanol-TPSR) (Fig. 8) experiments over α -Fe₂O₃ NSs and Au/ α -Fe₂O₃ NSs. Before the isopropanol-TPD experiment, α -Fe₂O₃ NSs and Au/ α -Fe₂O₃ NSs are pretreated by isopropanol pulse adsorption at room temperature, and then purged by 30 mL/min of He flow from room temperature to 900 °C. The fragment ions are detected by on-line mass spectrometry. Table 4 summarizes the relative strength of fragments for the possible compounds. Specially, the relative strength of fragments for isopropanol decreases in the order of (m/z = 45) > (m/z = 43) > (m/z = 41) > (m/z = 58) (Fig. S8). For isopropanol ((CH₃)₂CHOH) and acetone (CH₃COCH₃), the most abundant fragment is m/z = 45 and m/z = 43, respectively. Clearly, over α -Fe₂O₃ NSs, (CH₃)₂CHOH and CH₃COCH₃ are mainly desorbed at 66 and 237 °C, respectively. Over Au/ α -Fe₂O₃ NSs, the desorption peak of (CH₃)₂CHOH slightly shifts to low temperature (66 to 61 °C), and its intensity greatly decreases, while the desorption peak of CH₃COCH₃ begins to appear at 73–87 °C. Another characteristic fragment for CH₃COCH₃ is m/z = 58. The desorption profiles of m/z = 43 and m/z = 58 exhibit similar pattern. It should be noted that in addition to acetone, a number of intermediate

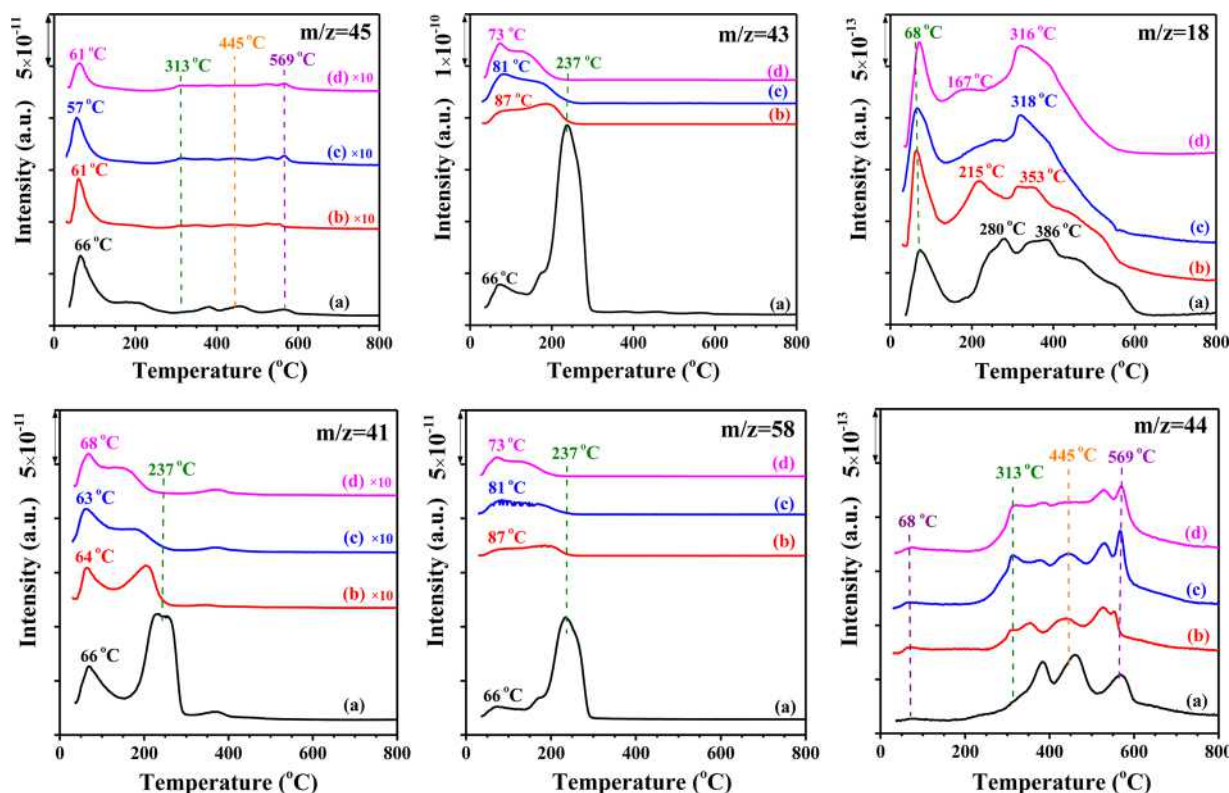


Fig. 7. Isopropanol-TPD profiles over (a) α -Fe₂O₃ NSs, (b) 0.38 wt% Au/ α -Fe₂O₃ NSs, (c) 0.81 wt% Au/ α -Fe₂O₃ NSs, and (d) 1.36 wt% Au/ α -Fe₂O₃ NSs.

products including acetic acid (CH₃COOH), 2-butanone (CH₃COCH₂CH₃), isopropyl acetate (CH₃COOCH(CH₃)₂), methyl vinyl ketone (CH₃COCH = CH₂), 3-penten-2-one (CH₃COCH = CHCH₃), acetaldehyde (CH₃CHO), isopropyl propionate (CH₃CH₂COOCH(CH₃)₂), isopropyl acrylate (CH₂=CHCOOCH(CH₃)₂), and isopropyl ether ((CH₃)₂CHOCH(CH₃)₂) also could produce large quantity of fragment of $m/z = 43$ (Table 4). In other words, the desorption peak of $m/z = 43$ detected in the range of room temperature to 300 °C could not ignore the contribution of intermediate product desorption. The fragment of $m/z = 41$ might be the characteristic ion fragment of 3-

penten-2-one (CH₃COCH = CHCH₃) and/or propylene (CH₂=CHCH₃). As shown in Fig. S9, the propylene selectivity over α -Fe₂O₃ NSs and 1.36 wt% Au/ α -Fe₂O₃ NSs is less than 2%. At T90 %, 3-penten-2-one is clearly observed over α -Fe₂O₃ NSs, and not found over 1.36 wt% Au/ α -Fe₂O₃ NSs (Fig. 5b and Fig. 5d). Therefore, the weak desorption peak of $m/z = 41$ over Au/ α -Fe₂O₃ NSs is mainly due to the propylene desorption, while that over α -Fe₂O₃ NSs is due to the 3-penten-2-one (CH₃COCH = CHCH₃) and/or propylene desorption. The fragment of $m/z = 18$ and $m/z = 44$ might be the characteristic ion fragment of H₂O and CO₂, respectively. Over α -Fe₂O₃ NSs and Au/ α -Fe₂O₃ NSs, a

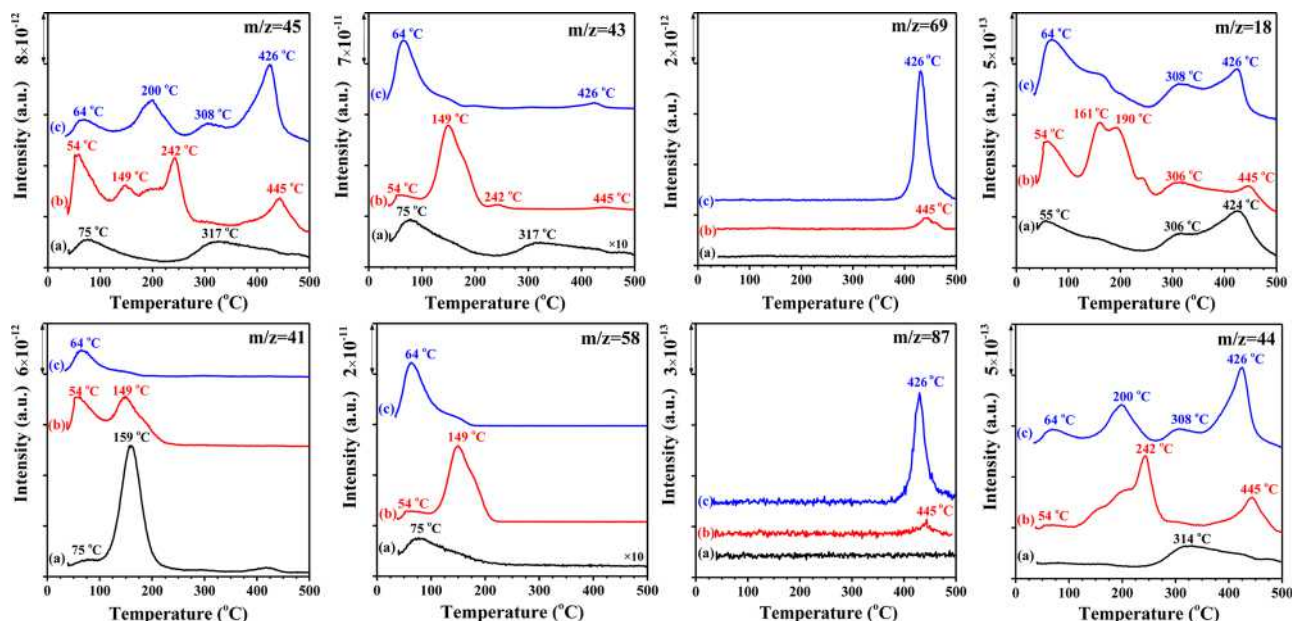


Fig. 8. Isopropanol-TPSR profiles over (a) commercial α -Fe₂O₃, (b) α -Fe₂O₃ NSs, and (c) 1.36 wt% Au/ α -Fe₂O₃ NSs.

Table 4
The relative strength of fragment ions for different compounds.

Compound	Molecular formula	m/z													
		18	41	43	44	45	55	57	58	59	69	72	87	96	
isopropanol	(CH ₃) ₂ CHOH		10	20		100			2						
acetone	CH ₃ COCH ₃		3	100					25						
propylene	CH ₂ =CHCH ₃		100												
acetic acid	CH ₃ COOH		3	100	3	91									
acetaldehyde	CH ₃ CHO		6	48	82	10									
methyl vinyl ketone	CH ₃ COCH = CH ₂			65	3		100								
2-butanone	CH ₃ COCH ₂ CH ₃			100								25			
isopropyl ether	(CH ₃) ₂ CHOHC(CH ₃) ₂		12	39	5	100				11	4		25		
isopropyl acetate	CH ₃ COOCH(CH ₃) ₂		18	100	5	5				17			25		
3-penten-2-one	CH ₃ COCH = CHCH ₃		95	55	3						100				
isopropyl acrylate	CH ₂ =CHCOOCH(CH ₃) ₂			30			100			15					
isopropyl propionate	CH ₃ CH ₂ COOCH(CH ₃) ₂			48				100		12					
2, 4-dimethylfuran	–		25											100	
carbon dioxide	CO ₂				100	3									
water	H ₂ O	100													

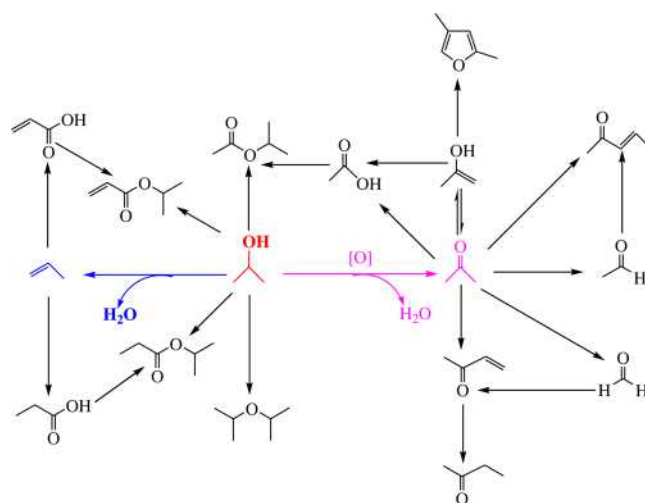
sharp desorption peak of $m/z = 18$ is detected at 68 °C, due to the selective catalytic oxidation of isopropanol, while that is detected in the range of 150–600 °C, due to the complete catalytic oxidation of reactants and products. In addition, the desorption peak of $m/z = 44$, due to the complete catalytic oxidation, is mainly observed in the range of 300–600 °C. Such results are consistent with the results of catalytic performance (Figs. S5, S6 and S9). Over the present catalysts and under the adopted reaction conditions, selective catalytic oxidation mainly occurs in the low temperature region, while complete catalytic oxidation mainly occurs in the high temperature region.

Before the isopropanol-TPSR experiment, commercial α -Fe₂O₃, α -Fe₂O₃ NSs and Au/ α -Fe₂O₃ NSs are pretreated by isopropanol pulse adsorption at room temperature, and then purged by 30 mL/min of 20 % O₂-80 % He (v/v) mixture from room temperature to 500 °C. Isopropanol-TPSR results are shown in Fig. 8 and Fig. S10. Over commercial α -Fe₂O₃, the strong peaks are detected at $m/z = 45$, 41, 44, and 18, as well as at $m/z = 59$, 57, and 55. The weak peaks are detected at $m/z = 43$ and 58. As shown in Fig. S7 and Fig. 5c, propylene (CH₂=CHCH₃) is the main product, in addition to little acetone and isopropyl ether ((CH₃)₂CHOHC(CH₃)₂) over commercial α -Fe₂O₃. Therefore, the desorption peak of $m/z = 45$ at 75 and 317 °C is due to isopropanol and isopropyl ether desorption, respectively. The desorption peak of $m/z = 41$ at 159 °C is due to propylene desorption. The desorption peaks of $m/z = 43$ and 58 at 75 °C are due to acetone desorption, and that of $m/z = 43$ at 317 °C is due to isopropyl ether desorption. Furthermore, no obvious signal of $m/z = 44$ due to CO₂ is detected at a temperature less than 250 °C, indicating complete catalytic oxidation reaction does not happen in the low temperature region. Over α -Fe₂O₃ NSs and 1.36 wt% Au/ α -Fe₂O₃ NSs, the signals are detected at $m/z = 45$, 43, 69, 41, 58, 87, 55, 57, 59, 72, 44, and 18. On the basis of the intermediate products detected by GC-MS (Fig. 5a, b, and d) and *in situ* DRIFTS (Fig. 6c–f), we roughly deduce that the desorption peaks of $m/z = 45$ at 54 or 64 °C are due to isopropanol desorption, while that in the range of 149–445 °C is due to acetic acid (CH₃COOH) and isopropyl ether ((CH₃)₂CHOHC(CH₃)₂) desorption. The desorption peaks of $m/z = 43$ and 58 are due to acetone desorption, and the temperature of desorption peak greatly decreases from 149 °C over α -Fe₂O₃ NSs to 64 °C over 1.36 wt% Au/ α -Fe₂O₃ NSs. The peaks of $m/z = 55$, 57, 59 and 87, 41 and 69, 72 are due to the methyl vinyl ketone (CH₃COCH=CH₂)/isopropyl acrylate (CH₂=CHCOOCH(CH₃)₂), isopropyl propionate (CH₃CH₂COOCH(CH₃)₂), isopropyl ether ((CH₃)₂CHOHC(CH₃)₂) and isopropyl acetate (CH₃COOCH(CH₃)₂), 3-penten-2-one (CH₃COCH=CHCH₃), 2-butanone (CH₃COCH₂CH₃) desorption, respectively. The temperature of desorption peak decreases, and/or the intensity of desorption peak increases over 1.36 wt% Au/ α -Fe₂O₃ NSs are due to the higher selective catalytic activity of the

supported Au catalyst (Fig. S5). In addition, the attribution of the peaks at $m/z = 18$ and 44 observed in the isopropanol-TPSR profiles is similar to that in the isopropanol-TPD profiles (Fig. 7).

3.6. The possible reaction mechanism for the selective catalytic oxidation of isopropanol to acetone over commercial α -Fe₂O₃, α -Fe₂O₃ NSs, and x wt% Au/ α -Fe₂O₃ NSs

Based on the results of GC-MS (Fig. 5), *in situ* DRIFTS (Fig. 6), isopropanol-TPD (Figs. 7 and S8), and isopropanol-TPSR (Figs. 8 and S10), we propose the possible reactions occur during the selective catalytic oxidation of isopropanol to acetone over the present catalysts (Scheme 1). Although α -Fe₂O₃ NSs and 1.36 wt% Au/ α -Fe₂O₃ NSs exhibit high selectivity to acetone, a number of products are detected. Propylene (CH₂=CHCH₃) is generated from the intramolecular dehydration reaction of isopropanol ((CH₃)₂CHOH), while isopropyl ether ((CH₃)₂CHOHC(CH₃)₂) is generated from the intermolecular dehydration reaction of isopropanol. Under certain reaction conditions, propylene (CH₂=CHCH₃) could be partially oxidized into acrylic acid (CH₂=CHCOOH) and propionic acid (CH₃CH₂COOH). Isopropyl acrylate (CH₂=CHCOOCH(CH₃)₂) and isopropyl propionate (CH₃CH₂COOCH(CH₃)₂) might be generated from the esterification reaction between acrylic acid (CH₂=CHCOOH) or propionic acid (CH₃CH₂COOH) and isopropanol ((CH₃)₂CHOH). 3-Penten-2-one



Scheme 1. Possible reactions occur during the selective catalytic oxidation of isopropanol to acetone over the present catalysts.

($\text{CH}_3\text{COCH} = \text{CHCH}_3$) is generated from the aldol condensation reaction between acetaldehyde (CH_3CHO) and acetone (CH_3COCH_3). Isopropyl acetate ($\text{CH}_3\text{COOCH}(\text{CH}_3)_2$) is generated from the esterification reaction between acetic acid (CH_3COOH) and isopropanol ($(\text{CH}_3)_2\text{CHOH}$). The isomerization of acetone (CH_3COCH_3) could generate less stable allyl alcohol ($\text{CH}_2 = \text{COHCH}_3$). On one hand, allyl alcohol might be further oxidized into small molecules, including acetaldehyde (CH_3CHO), acetic acid (CH_3COOH), and formaldehyde (HCHO). On the other hand, the keto-enol tautomerism of acetone (CH_3COCH_3) and allyl alcohol ($\text{CH}_2 = \text{COHCH}_3$) would cause the generation of 2, 4-dimethylfuran. Methyl vinyl ketone ($\text{CH}_3\text{COCH} = \text{CH}_2$) might be obtained from the condensation reaction between formaldehyde (HCHO) and acetone (CH_3COCH_3), and 2-butanone ($\text{CH}_3\text{COCH}_2\text{CH}_3$) might be obtained from the selective hydrogenation of methyl vinyl ketone ($\text{CH}_3\text{COCH} = \text{CH}_2$). Of course, the proposed reaction mechanism needs further investigation, considering the presence of various active species (e.g. $\text{CH}_2 = \text{C}(\text{CH}_3) = \text{O}_{(\text{ads})}$, CH_3CHO^* , CH_2O^* and $\text{COO}_{(\text{ads})}$) generated from the catalytic oxidation process [41].

3.7. Influence of reactant composition and moisture on catalytic activity, selectivity, and stability of 1.36 wt% Au/ α - Fe_2O_3 NSs

Considering the possible application background in the semiconductor industry, isopropanol is directly converted to acetone and then recycled. The 0.1 vol% concentration of isopropanol is relatively low, and far away from the practical demand. On the other hand, the explosive limit of isopropanol is in the range of 2–12 vol%. On the basis of the balance between demand and safety, we further evaluate the catalytic performance of 1.36 wt% Au/ α - Fe_2O_3 NSs for selective catalytic oxidation of isopropanol under the reactants consisted of 0.75 vol% or 1.2 vol% isopropanol, and 40 vol% or 10 vol% O_2 . Generally, more isopropanol and less O_2 would depress the complete oxidation reaction to some extent. 1.36 wt% Au/ α - Fe_2O_3 NSs does not exhibit much difference in the catalytic performance in the presence of 0.75 vol% isopropanol and 40 vol% O_2 , 1.2 vol% isopropanol and 40 vol% O_2 , 0.75 vol% isopropanol and 10 vol% O_2 , or 1.2 vol% isopropanol and 10 vol% O_2 (Fig. S9). In the range of 60–220 °C, isopropanol conversion increases with a rise in temperature, and the temperature required for 90 % (T90 %) conversion of isopropanol is about 180 °C. The major product is acetone, and acetone selectivity is more than 90 % even at 220 °C. Under the condition of different reactant compositions, a small amount of propylene is detected in addition to acetone. The propylene selectivity over α - Fe_2O_3 NSs or 1.36 wt% Au/ α - Fe_2O_3 NSs is less than 2% (Fig. S9C). In the high temperature reaction region, propylene selectivity over 1.36 wt% Au/ α - Fe_2O_3 slightly increases with a rise in isopropanol concentration, and a decrease in O_2 concentration. In the presence of 1.2 vol% isopropanol and 40 vol% O_2 , acetone selectivity and yield over 1.36 wt% Au/ α - Fe_2O_3 NSs could be as high as about 99 % and 95 % at 220 °C, respectively.

We also investigate the moisture effect. Generally, isopropanol conversion, acetone selectivity and yield, as well as CO_2 selectivity at a reaction temperature higher than 90 °C do not exhibit much difference at different relative humidities of 25 %, 50 %, 75 %, and 100 % over 1.36 wt% Au/ α - Fe_2O_3 NSs (Fig. 9). At a low reaction temperature of 60 °C (Table 5), the presence of little water vapor (relative humidity = 25 %, 50 %, and 75 %) enhances the conversion of isopropanol, while the presence of large water vapor (relative humidity = 100 %) obviously decreases the conversion of isopropanol due to the competitive adsorption. At 60 °C, TOF_{Au} under 0 – 75 % of relative humidity is in the range of $44.9 - 68.6 (\times 10^{-3} \text{ s}^{-1})$, larger than that ($7.1 \times 10^{-3} \text{ s}^{-1}$) under 100 % of relative humidity. Isopropanol consumption rate and acetone formation rate also show similar changing trend to TOF_{Au} . It should be noted that at a reaction temperature lower than 250 °C, acetone selectivity could be kept more than 90 %, and CO_2 selectivity is less than 5%. However, acetone selectivity greatly decreases and CO_2

selectivity obviously increases at 280 °C.

Catalytic stability is another important factor for the practical application. The present selective catalytic oxidation of isopropanol is carried out in an oxygen rich atmosphere, and maintaining the acetone selectivity and yield at a high level is relatively difficult. We herein further investigate the catalytic stability of 1.36 wt% Au/ α - Fe_2O_3 NSs under various reaction temperatures and reactant compositions. In the presence of 0.1 vol% isopropanol and 40 vol% O_2 (Fig. S11a), isopropanol conversion decreases from 60 % to 50 %, acetone selectivity slightly decreases from 96 % to 91 %, and acetone yield decreases from 58 % to 46 %, after continues reaction at 45 °C (the temperature required for 60 % conversion of isopropanol, T60 %) for 10 h. The possible reason for the decrease in conversion, selectivity, and yield is due to the competitive adsorption of isopropanol and acetone at low temperatures. Actually, the isopropanol conversion, acetone selectivity and yield well remain after continuous reaction at 120 °C (the temperature required for 90 % conversion of isopropanol, T90 %) for 10 h (Fig. S11b). From Fig. S11c and Fig. S11d, the catalytic stability of 1.36 wt% Au/ α - Fe_2O_3 NSs at ca. T90 % is very good within 30 h on-stream reaction time, in the presence of 0.75 vol% isopropanol and 10 vol% O_2 , or 1.2 vol% isopropanol and 40 vol% O_2 . High acetone selectivity (95–97 %) and yield (93–95 %) could be obtained even at 220 °C under 100 % of relative humidity (Fig. 10). Usually, particle aggregation, carbon deposition, crystal phase transformation, and change in surface composition could cause the deactivation of a supported noble metal catalyst. Therefore, we believe that the crystal structure and surface composition of the 1.36 wt% Au/ α - Fe_2O_3 NSs catalyst would not be changed under the adopted reaction conditions.

3.8. The possible reasons for the better catalytic performance of 1.36 wt% Au/ α - Fe_2O_3 NSs

Isopropanol could be converted to propylene by dehydration, and to acetone by dehydrogenation or oxidative dehydrogenation. Previously, it was found that isopropanol dehydrogenation could happen over anatase TiO_2 , and increasing surface –OH and oxygen partial pressure benefited dehydrogenation rate, while not affected dehydration rate [42]. The deposition of Pd onto the surface of TiO_2 might change the reaction pathway of propanol decomposition, and caused the generation of propylene and acetone [43]. Under the present reaction conditions, the dehydration reaction ($(\text{CH}_3)_2\text{CHOH} \rightarrow \text{CH}_2 = \text{CHCH}_3 + \text{H}_2\text{O}$) mainly proceeds over commercial Fe_2O_3 (Fig. S7), while the oxidative dehydrogenation reaction ($(\text{CH}_3)_2\text{CHOH} + \text{O}_2 \rightarrow \text{CH}_3\text{COCH}_3 + \text{H}_2\text{O}$) mainly proceeds over α - Fe_2O_3 NSs and Au/ α - Fe_2O_3 NSs (Figs. S5 and S9) [44]. It has been reported that strong acidic and weak basic sites benefit the dehydration of isopropanol to propylene, while moderate acidic and strong basic sites benefit the dehydrogenation of isopropanol to acetone [44,45]. Based on the results of NH_3 -TPD and pyridine-*in situ* DRIFTS experiments (Figs. 3 and 4, Table 2), we find that the NH_3 desorption temperature decreases, and the NH_3 desorption amount increases in order of commercial α - Fe_2O_3 , α - Fe_2O_3 NSs, and 1.36 wt% Au/ α - Fe_2O_3 NSs, and the ratio of Brønsted acidic sites to Lewis acidic sites decreases in order of α - Fe_2O_3 NSs, commercial α - Fe_2O_3 , and 1.36 wt% Au/ α - Fe_2O_3 NSs. The NH_3 desorption temperature and amount, as well as the ratio of Brønsted acidic sites to Lewis acidic sites, indicate the acid strength and amount. In other words, commercial α - Fe_2O_3 possesses more strong acidic sites, while α - Fe_2O_3 NSs and 1.36 wt% Au/ α - Fe_2O_3 NSs possess more moderate acidic sites. In addition to the acidic sites, the redox property might also play an important role in the selective or complete catalytic oxidation of propanol [45,46]. Liu and Yang [45] investigated the complete oxidation of isopropanol over CeO_2 , Fe_2O_3 , TiO_2 , and Al_2O_3 supported Au catalysts, and found that Au/ CeO_2 indicated higher activity due to its better redox and basic properties. The loading of Au NPs onto the surface of CeO_2 weakened the bonds of Ce – O nearby Au atoms, and then increased the mobility of the surface reactive lattice oxygen species. Gong et al. [46] reported

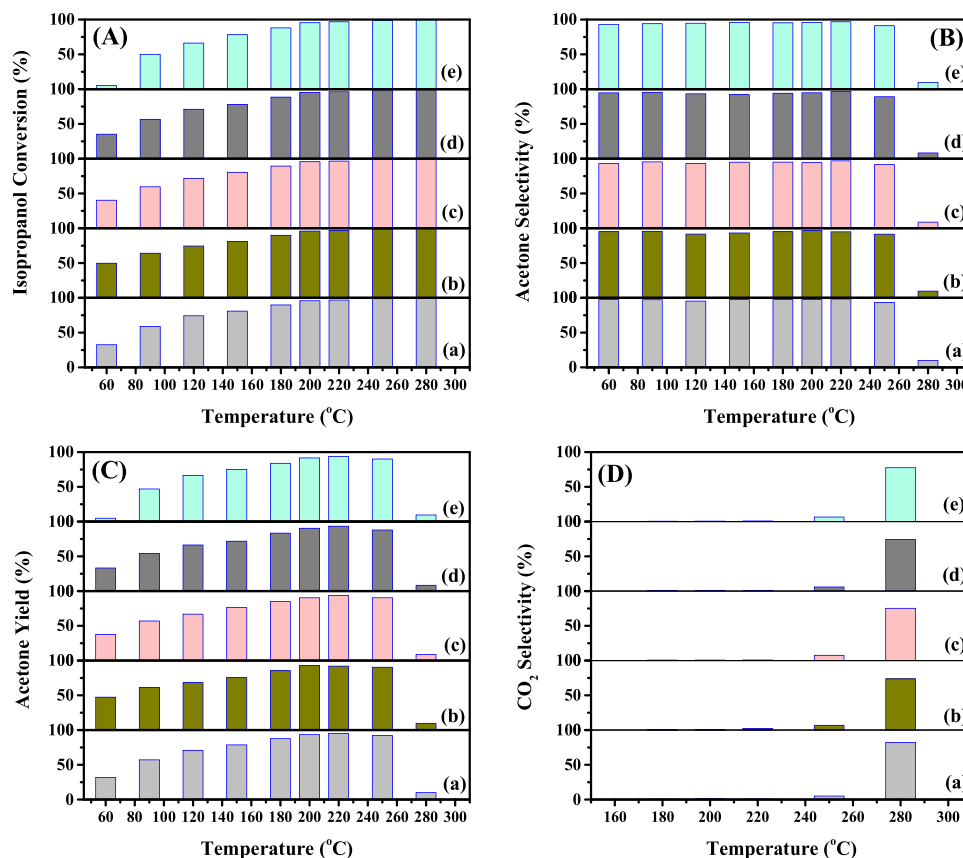


Fig. 9. Isopropanol conversion (A), acetone selectivity (B) and yield (C), CO₂ selectivity (D) as a function of reaction temperature over 1.36 wt% Au/α-Fe₂O₃ NSs with the reactants composed of 1.2 vol% isopropanol and 40 vol% O₂ at different relative humidity: (a) 0%, (b) 25 %, (c) 50 %, (d) 75 %, and (e) 100 %.

that pre-covered atomic oxygen on Au(111) could act as a Brønsted base for the first hydrogen abstraction. The dehydrogenation of isopropanol proceeded according to the cleavage of O–H bond, and then the selective activation of β-C–H bond. The cleavage of C – O bond did not happen, and the cleavage of non-selective γ-C–H bond was inhibited due to the atomic oxygen pre-covered Au(111). Finally, high selectivity to acetone could be achieved. The possible mechanism for molecular oxygen activation over the metal oxide supported Au catalyst involves O₂ dissociation on the surface oxygen vacancies, and the generation of oxygen atoms. We herein find that defect sites (including oxygen vacancy) increase on the support after the modification of Au NPs from the results of XRD (Fig. S1) and ⁵⁷Fe-Mössbauer (Fig. 1) characterizations. From the results of XPS characterization (Fig. S4 and Table 1), we find that the loading of Au NPs onto α-Fe₂O₃ NSs causes an interaction ($\text{Au}^0 + \text{Fe}^{3+} \rightarrow \text{Au}^{\delta+} + \text{Fe}^{2+}$), and weakens the bonds of Fe – O nearby Au atoms. Furthermore, the surface O_{ads}/O_{latt} molar ratio increases from 0.24 to 0.38 with a rise in the Au loading from 0 to 1.36 wt %. Usually, the O_{ads} species are adsorbed on the oxygen vacancies [47]. In other words, the 1.36 wt% Au/α-Fe₂O₃ NSs catalyst possesses larger oxygen vacancies. The morphology of the support might influence the

catalytic performance of Au/α-Fe₂O₃ nanocatalysts. The present α-Fe₂O₃ nanosheets support mainly expose the (110) crystal plane (Fig. S2), with larger Fe atom density and oxygen vacancy concentration [22,48–50]. From the results of H₂-TPR characterization (Fig. 2), the interaction between Au NPs and α-Fe₂O₃ NSs is further confirmed, since the temperature of the initial reduction peak shifts to low temperature with a rise in the Au loading. Therefore, the excellent catalytic performance of 1.36 wt% Au/α-Fe₂O₃ NSs for the selective catalytic oxidation of isopropanol to acetone is due to the presence of moderate acidic sites, larger surface oxygen vacancies, and better low-temperature reducibility [19,27,32,45,46].

4. Conclusions

Generally, we fabricate α-Fe₂O₃ NSs and their supported 0.38, 0.81, and 1.36 wt% Au nanocatalysts via the solvothermal and colloidal deposition method, respectively. The α-Fe₂O₃ nanocrystals display regular hexagonal morphology, and the width and thickness are about 180 and 15 nm, respectively. Au NPs (average particle size = 4.0 nm) are well dispersed on the surface of α-Fe₂O₃ NSs. Commercial α-Fe₂O₃ possesses

Table 5

Isopropanol conversion and consumption rate; acetone selectivity, yield, and formation rate; and TOF_{Au} at 60 °C for the selective catalytic oxidation of 1.2 vol% isopropanol over 1.36 wt% Au/α-Fe₂O₃ under different relative humidity.

Relative humidity (%)	Isopropanol conversion (%)	Acetone selectivity (%)	Acetone yield (%)	TOF _{Au} (× 10 ^{−3} s ^{−1})	Isopropanol consumption rate (× 10 ^{−7} mol/(g _{cat} s))	Acetone formation rate (× 10 ^{−7} mol/(g _{cat} s))
0	32.5	97.8	31.8	44.9	8.9	8.6
25	49.7	95.2	47.3	68.6	13.5	12.9
50	40.2	93.3	37.5	55.5	10.9	10.2
75	35.1	94.6	33.2	48.4	9.6	9.1
100	5.2	92.3	4.8	7.1	1.4	1.3

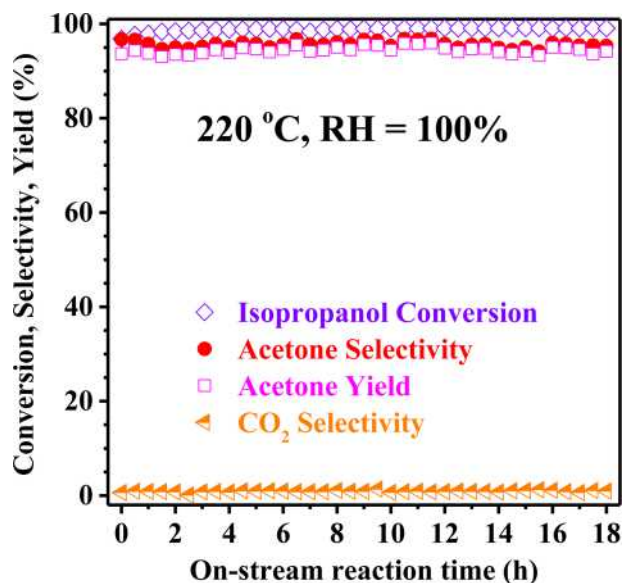


Fig. 10. The catalytic stability of 1.36 wt% Au/ α -Fe₂O₃ NSs for the selective catalytic oxidation of isopropanol at 100 % of relative humidity as a function of reaction time.

more strong acidic sites, while α -Fe₂O₃ NSs and 1.36 wt% Au/ α -Fe₂O₃ NSs possess more moderate acidic sites. The loading of Au NPs onto α -Fe₂O₃ NSs weakens the Fe – O bonds, increases the surface oxygen vacancies, and enhances the low-temperature reducibility. 1.36 wt% Au/ α -Fe₂O₃ NSs exhibits excellent catalytic performance for the selective catalytic oxidation of isopropanol to acetone. In the presence of 1.2 vol% isopropanol and 40 vol% O₂, acetone selectivity and yield over 1.36 wt% Au/ α -Fe₂O₃ NSs could be as high as 99 % and 95 % at 220 °C, respectively. In addition to acetone, a number of organic compounds, including propylene, acetic acid, acetaldehyde, methyl vinyl ketone, 2-butanone, isopropyl ether, isopropyl acetate, 3-penten-2-one, isopropyl acrylate, isopropyl propionate, and 2, 4-dimethylfuran are detected. The possible reaction mechanism is proposed for the selective catalytic oxidation of isopropanol to acetone over the present catalysts. We believe the selective catalytic oxidation method, rather than the complete catalytic oxidation method, provides an alternative and economic method for VOCs emissions control.

5. Credit author statement

Honghong Zhang carried out experiments, wrote and modified the manuscript.

Lingyun Dai modified the manuscript.

Yuan Feng and Yuhang Xu carried out some experiments.

Yuxi Liu, Guangsheng Guo, Hongxing Dai, Chongchen Wang, Can Wang, Hsing-Cheng Hsi, and Haibao Huang analyzed the experimental results.

Jiguang Deng designed the experiments, analyzed the experimental results, wrote and modified the manuscript.

Acknowledgements

This work is supported by the Natural Science Foundation of China (21622701, 21961160743, U1507108, and 21477005) and the National Key R&D Program of China(2016YFC0204800). We sincerely thank the School of Physical Science and Technology of Lanzhou University for the Mössbauer characterization.

Appendix A. Supplementary data

Supplementary material related to this article can be found, in the online version, at doi:<https://doi.org/10.1016/j.apcatb.2020.119011>.

References

- [1] K.H. Chiu, B.Z. Wu, C.C. Chang, U. Sree, J.G. Lo, Distribution of volatile organic compounds over a semiconductor industrial park in Taiwan, *Environ. Sci. Technol.* 39 (2005) 973–983.
- [2] S. Choi, C. Yoon, S. Kim, W. Kim, K. Ha, J. Jeong, J. Kim, J. Shin, D. Park, Comprehensive evaluation of hazardous chemical exposure control system at a semiconductor manufacturing company in South Korea, *Int. J. Environ. Res. Public Health* 15 (2018) 1162.
- [3] J.G. Deng, S.N. He, S.H. Xie, H.G. Yang, Y.X. Liu, G.S. Guo, H.X. Dai, Ultralow loading of silver nanoparticles on Mn₂O₃ nanowires derived with molten salts: A high-efficiency catalyst for the oxidative removal of toluene, *Environ. Sci. Technol.* 49 (2015) 11089–11095.
- [4] J. Chen, X. Chen, W.J. Xu, Z. Xu, H.P. Jia, J. Chen, Homogeneous introduction of CeO₂ into MnO₂-based catalyst for oxidation of aromatic VOCs, *Appl. Catal. B* 224 (2018) 825–835.
- [5] P.M. Shah, A.N. Day, T.E. Davies, D.J. Morgan, S.H. Taylor, Mechanochemical preparation of ceria-zirconia catalysts for the total oxidation of propane and naphthalene volatile organic compounds, *Appl. Catal. B* 253 (2019) 331–340.
- [6] Z.W. Wang, S. Li, S.H. Xie, Y.X. Liu, H.X. Dai, G.S. Guo, J.G. Deng, Supported ultralow loading Pt catalysts with high H₂O-, CO₂-, and SO₂-resistance for acetone removal, *Appl. Catal. A Gen.* 579 (2019) 106–115.
- [7] W.B. Pei, Y.X. Liu, J.G. Deng, K.F. Zhang, Z.Q. Hou, X.T. Zhao, H.X. Dai, Partially embedding Pt nanoparticles in the skeleton of 3DOM Mn₂O₃: An effective strategy for enhancing catalytic stability in toluene combustion, *Appl. Catal. B* 256 (2019) 117814.
- [8] S.H. Xie, H.X. Dai, J.G. Deng, H.G. Yang, W. Han, H. Arandiyani, G.S. Guo, Preparation and high catalytic performance of Au/3DOM Mn₂O₃ for the oxidation of carbon monoxide and toluene, *J. Hazard. Mater.* 279 (2014) 392–401.
- [9] R.S. Peng, S.J. Li, X.B. Sun, Q.M. Ren, L.M. Chen, M.L. Fu, J.L. Wu, D.Q. Ye, Size effect of Pt nanoparticles on the catalytic oxidation of toluene over Pt/CeO₂ catalysts, *Appl. Catal. B* 220 (2018) 462–470.
- [10] X. Zhang, Y.X. Liu, J.G. Deng, X.H. Yu, Z. Han, K.F. Zhang, H.X. Dai, Alloying of gold with palladium: An effective strategy to improve catalytic stability and chlorine-tolerance of the 3DOM CeO₂-supported catalysts in trichloroethylene combustion, *Appl. Catal. B* 257 (2019) 117879.
- [11] H.F. Xiong, M.H. Wiebenga, C. Carrillo, J.R. Gaudet, H.N. Pham, D. Kunwar, S.H. Oh, G. Qi, C.H. Kim, A.K. Datye, Design considerations for low-temperature hydrocarbon oxidation reactions on Pd based catalysts, *Appl. Catal. B* 236 (2018) 436–444.
- [12] M. Haruta, S. Tsubota, T. Kobayashi, H. Kageyama, M.J. Genet, B. Delmon, Low-temperature oxidation of CO over gold supported on TiO₂, α -Fe₂O₃, and Co₃O₄, *J. Catal.* 144 (1993) 175–192.
- [13] J. Saavedra, C.J. Pursell, B.D. Chandler, CO oxidation kinetics over Au/TiO₂ and Au/Al₂O₃ catalysts: evidence for a common water-assisted mechanism, *J. Am. Chem. Soc.* 140 (2018) 3712–3723.
- [14] M. González-Castaño, T.R. Reina, S. Ivanova, L.M. Tejada Martínez, M.A. Centeno, J.A. Odriozola, O₂-assisted water gas shift reaction over structured Au and Pt catalysts, *Appl. Catal. B* 185 (2016) 337–343.
- [15] W. Han, J.G. Deng, S.H. Xie, H.G. Yang, H.X. Dai, C.T. Au, Gold supported on iron oxide nanodisk as efficient catalyst for the removal of toluene, *Ind. Eng. Chem. Res.* 53 (2014) 3486–3494.
- [16] L.P. Zeng, K.Z. Li, H. Wang, H. Yu, X. Zhu, Y.G. Wei, P.H. Ning, C.Z. Shi, Y.M. Luo, CO oxidation on Au/ α -Fe₂O₃-hollow catalysts: General synthesis and structural dependence, *J. Phys. Chem. C* 121 (2017) 12696–12710.
- [17] J.T. Li, L.W. Wang, Z. Liu, Y.H. Wang, S.L. Wang, Au-modified α -Fe₂O₃ columnar superstructures assembled with nanoplates and their highly improved acetone sensing properties, *J. Alloys. Compd.* 728 (2017) 944–951.
- [18] Y. Li, W.J. Shen, Morphology-dependent nanocatalysts: rod-shaped oxides, *Chem. Soc. Rev.* 43 (2014) 1543–1574.
- [19] S. Minicò, S. Scirè, C. Crisafulli, R. Maggiore, S. Galvagno, Catalytic combustion of volatile organic compounds on gold/iron oxide catalysts, *Appl. Catal. B* 28 (2000) 245–251.
- [20] Y.Z. Shen, Z.D. Zhu, X.G. Wang, J.Y. Gong, Y.R. Zhang, Synthesis of Z-scheme g-C₃N₄/Ag/Ag₃PO₄ composite for enhanced photocatalytic degradation of phenol and selective oxidation of gaseous isopropanol, *Mater. Res. Bull.* 107 (2018) 407–415.
- [21] K.F. Ortega, S. Anke, S. Salamon, F. Özcan, J. Heese, C. Andronescu, J. Landers, H. Wende, W. Schuhmann, M. Muhler, Topotactic synthesis of porous cobalt ferrite platelets from a layered double hydroxide precursor and their application in oxidation catalysis, *Chem. Eur. J.* 23 (2017) 12443–12449.
- [22] L.Q. Chen, X.F. Yang, J. Chen, J. Liu, H. Wu, H.Q. Zhan, C.L. Liang, M.M. Wu, Continuous shape- and spectroscopy-tuning of hematite nanocrystals, *Inorg. Chem.* 49 (2010) 8411–8420.
- [23] Y.X. Liu, H.X. Dai, J.G. Deng, S.H. Xie, H.G. Yang, W. Tan, W. Han, Y. Jiang, G.S. Guo, Mesoporous Co₃O₄-supported gold nanocatalysts: Highly active for the oxidation of carbon monoxide, benzene, toluene, and o-xylene, *J. Catal.* 309 (2014) 408–418.
- [24] O.M. Lemine, Microstructural characterisation of α -Fe₂O₃ nanoparticles using XRD line profiles analysis, FE-SEM and FT-IR, *Superlattice. Microsc.* 45 (2009) 576–582.

- [25] G. Bhargava, I. Gouzman, C.M. Chun, T.A. Ramanarayanan, S.L. Bernasek, Characterization of the “native” surface thin film on pure polycrystalline iron: A high resolution XPS and TEM study, *Appl. Surf. Sci.* 253 (2007) 4322–4329.
- [26] T. Yamashita, P. Hayes, Analysis of XPS spectra of Fe^{2+} and Fe^{3+} ions in oxide materials, *Appl. Surf. Sci.* 254 (2008) 2441–2449.
- [27] K. Yang, Y.X. Liu, J.G. Deng, X.T. Zhao, J. Yang, Z. Han, Z.Q. Hou, H.X. Dai, Three-dimensionally ordered mesoporous iron oxide-supported single-atom platinum: highly active catalysts for benzene combustion, *Appl. Catal. B* 244 (2019) 650–659.
- [28] Y.J. Liang, Y.X. Liu, J.G. Deng, K.F. Zhang, Z.Q. Hou, X.T. Zhao, X. Zhang, K.Y. Zhang, R.J. Wei, H.X. Dai, Coupled palladium–tungsten bimetallic nanosheets/ TiO_2 hybrids with enhanced catalytic activity and stability for the oxidative removal of benzene, *Environ. Sci. Technol.* 53 (2019) 5926–5935.
- [29] Q.G. Dai, Q. Zhu, Y. Lou, X.Y. Wang, Role of Brønsted acid site during catalytic combustion of methane over $\text{PdO}/\text{ZSM-5}$: dominant or negligible? *J. Catal.* 357 (2018) 29–40.
- [30] M.A. Ardagh, Z. Bo, S.L. Nauert, J.M. Notestein, Depositing SiO_2 on Al_2O_3 : A route to tunable Brønsted acid catalysts, *ACS Catal.* 6 (2016) 6156–6164.
- [31] J.F. Wu, T.M. Su, Y.X. Jiang, X.L. Xie, Z.Z. Qin, H.B. Ji, In situ DRIFTS study of O_3 adsorption on CaO , $\gamma\text{-Al}_2\text{O}_3$, CuO , $\alpha\text{-Fe}_2\text{O}_3$ and ZnO at room temperature for the catalytic ozonation of cinnamaldehyde, *Appl. Surf. Sci.* 412 (2017) 290–305.
- [32] R.M. Rioux, M.A. Vannice, Hydrogenation/dehydrogenation reactions: isopropanol dehydrogenation over copper catalysts, *J. Catal.* 216 (2003) 362–376.
- [33] G.S. Foo, F. Polo-Garzon, V. Fung, D.-E. Jiang, S.H. Overbury, Z.L. Wu, Acid–base reactivity of perovskite catalysts probed via conversion of 2-propanol over titanates and zirconates, *ACS Catal.* 7 (2017) 4423–4434.
- [34] X.Y. Chen, S.L. Chen, A.P. Jia, J.Q. Lu, W.X. Huang, Gas phase propylene epoxidation over Au supported on titanosilicates with different Ti chemical environments, *Appl. Surf. Sci.* 393 (2017) 11–22.
- [35] Y.N. Wang, W.H. Ma, D.Y. Wang, Q. Zhong, Study on the reaction mechanism of the propylene oxide rearrangement via in situ DRIFTS, *Chem. Eng. J.* 307 (2017) 1047–1054.
- [36] J. Liu, Q.D. Zhao, X.Y. Li, J.H. Chen, D.K. Zhang, Structure sensitivity of selective catalytic reduction of NO with propylene over Cu-doped $\text{Ti}_{0.5}\text{Zr}_{0.5}\text{O}_{2-\delta}$ catalysts, *Appl. Catal. B* 165 (2015) 519–528.
- [37] J. Song, K.J. Huang, N. Wang, Gas-sensing properties and in situ diffuse-reflectance Fourier-transform infrared spectroscopy study of diethyl ether adsorption and reactions on SnO_2/rGO film, *J. Mater. Res.* 31 (2016) 2035–2045.
- [38] R.M. Silverstein, F.X. Webster, D.J. Kiemle, D.L. Bryce, *Spectrometric Identification of Organic Compounds*, 8th edition, East China University of Science and Technology Press, Shanghai, 2017.
- [39] H. Zhou, W.L. Zhu, L. Shi, H.C. Liu, S.P. Liu, Y.M. Ni, Y. Liu, Y.L. He, S.L. Xu, L.N. Li, Z.M. Liu, In situ DRIFT study of dimethyl ether carbonylation to methyl acetate on H-mordenite, *J. Mol. Catal. A: Chem.* 417 (2016) 1–9.
- [40] Z.X. Jia, A. Rousseau, Sorbent track: quantitative monitoring of adsorbed VOCs under in-situ plasma exposure, *Sci. Rep.* 6 (2016) 31888.
- [41] Y.G. Sun, X. Zhang, N. Li, X. Xing, H.L. Yang, F.L. Zhang, J. Cheng, Z.S. Zhang, Z.P. Hao, Surface properties enhanced Mn_xAlO oxide catalysts derived from Mn_xAl layered double hydroxides for acetone catalytic oxidation at low temperature, *Appl. Catal. B* 251 (2019) 295–304.
- [42] J.E. Rekoske, M.A. Barteau, Kinetics and selectivity of 2-propanol conversion on oxidized anatase TiO_2 , *J. Catal.* 165 (1997) 57–72.
- [43] H. Bahruji, M. Bowker, C. Brookes, P.R. Davies, I. Wawata, The adsorption and reaction of alcohols on TiO_2 and Pd/TiO_2 catalysts, *Appl. Catal. A Gen.* 454 (2013) 66–73.
- [44] S. Anke, G. Bendt, I. Sinev, H. Hajiyani, H. Antoni, I. Zegkinoglou, H. Jeon, R. Pentcheva, C. Beatriz Roldan, S. Schulz, Selective 2-propanol oxidation over unsupported Co_3O_4 spinel nanoparticles: Mechanistic insights into aerobic oxidation of alcohols, *ACS Catal.* 9 (2019) 5974–5985.
- [45] S.Y. Liu, S.M. Yang, Complete oxidation of 2-propanol over gold-based catalysts supported on metal oxides, *Appl. Catal. A Gen.* 334 (2008) 92–99.
- [46] J.L. Gong, D.W. Flaherty, T. Yan, C.B. Mullins, Selective oxidation of propanol on Au(111): mechanistic insights into aerobic oxidation of alcohols, *ChemPhysChem* 9 (2008) 2461–2466.
- [47] C.Y. Ma, C.G. Yang, B. Wang, C. Chen, F.B. Wang, X.L. Yao, M.Y. Song, Effects of H_2O on HCHO and CO oxidation at room-temperature catalyzed by MCo_2O_4 ($\text{M} = \text{Mn}, \text{Ce}$ and Cu) materials, *Appl. Catal. B* 254 (2019) 76–85.
- [48] Y.H. Zheng, Y. Cheng, Y.S. Wang, F. Bao, L.H. Zhou, X.F. Wei, Y.Y. Zhang, Q. Zheng, Quasicubic $\alpha\text{-Fe}_2\text{O}_3$ nanoparticles with excellent catalytic performance, *J. Phys. Chem. B* 110 (2006) 3093–3097.
- [49] X.J. Liu, J.F. Liu, Z. Chang, X.M. Sun, Y.D. Li, Crystal plane effect of Fe_2O_3 with various morphologies on CO catalytic oxidation, *Catal. Commun.* 12 (2011) 530–534.
- [50] Y.F. Jian, T.T. Yu, Z.Y. Jiang, Y.K. Yu, M. Douthwaite, J.Y. Liu, R. Albilali, C. He, In-depth understanding of the morphology effect of $\alpha\text{-Fe}_2\text{O}_3$ on catalytic ethane destruction, *ACS Appl. Mater. Interfaces* 11 (2019) 11369–11383.